Estimation of Wind Conditions in the Offshore Direction Using Multiple Numerical Models and In Situ Observations

Konagaya, Mizuki ; Ohsawa, Teruo ; Itoshima, Yuki ; Kambayashi, Masaki ; Leonard, Edouard ; Tromeur, Eric ; Misaki, Takeshi ; Shintaku, Erika…

(Citation)
Energies,18(11):3000

(Issue Date)
2025-06-05

(Resource Type)
journal article

(Version)
Version of Record

energies

MDPI

Article

Estimation of Wind Conditions in the Offshore Direction Using Multiple Numerical Models and In Situ Observations

Mizuki Konagaya [1,2,*], Teruo Ohsawa [1], Yuki Itoshima [1], Masaki Kambayashi [1], Edouard Leonard [3], Eric Tromeur [3], Takeshi Misaki [1,2], Erika Shintaku [2], Ryuzo Araki [4] and Kohei Hamada [5]

1 Graduate School of Maritime Sciences, Kobe University, 5-1-1 Fukae-Minami, Higashinada-Ku, Kobe 658-0022, Hyogo, Japan; ohsawa@port.kobe-u.ac.jp (T.O.); t.misaki@people.kobe-u.ac.jp (T.M.)
2 Rera Tech Inc., 5-1-1 Fukae-Minami, Higashinada-Ku, Kobe 658-0022, Hyogo, Japan; e.shintaku@rera-tech.co.jp
3 Meteodyn, 7 et 9 Rue Duguay Trouin, Ilot 1 de la ZAC de la Baule, 44800 Saint-Herblain, France; edouard.leonard@meteodyn.com (E.L.); eric.tromeur@meteodyn.com (E.T.)
4 Japan Meteorological Corporation, Grand Front Osaka Tower-A 29F, 4-20 Ofukacho, Kita-Ku, Osaka 530-0011, Osaka, Japan; araki@n-kishou.co.jp
5 E&E Solutions Inc., Akihabara UDX Building, 14-1 Sotokanda 4-Chome, Chiyoda-Ku 101-0021, Tokyo, Japan; k-hamada@eesol.co.jp
* Correspondence: m.konagaya@port.kobe-u.ac.jp; Tel.: +81-90-2529-9612

Abstract: This study aims to estimate nearshore wind conditions using multiple numerical models and evaluate their accuracy at heights relevant to offshore wind turbines. An intensive observation campaign was conducted from December 2021 to February 2022 at Mutsu Ogawara Port, Japan. The observed data were used to validate the accuracy of numerical models (mesoscale, computational fluid dynamics (CFD), and linear models) to estimate wind conditions and investigate thermal environments, including atmospheric stability. The results demonstrated that the accuracy of period-averaged wind speed estimation in the offshore direction improved significantly when using an offshore observation point as a reference, with biases within ±2.5% up to 5 km offshore for all models. However, the accuracy of vertical shear estimation varies widely among models, with several models overestimating vertical shear, particularly in the sea wind sector. The mesoscale model, which accounts for spatiotemporal variations in atmospheric stability, consistently achieves high estimation accuracy. In contrast, standalone CFD models, which typically assume neutral atmospheric stability, are difficult to estimate accurately. Nonetheless, incorporating specific atmospheric stability conditions into the CFD models significantly enhanced their accuracy. These findings underscore the importance of atmospheric stability when estimating offshore wind conditions, particularly in nearshore areas.

Keywords: offshore wind energy; nearshore waters; wind resource assessment; CFD model; mesoscale model; atmospheric stability

Academic Editor: Yaqing Jin

Received: 30 April 2025
Revised: 25 May 2025
Accepted: 28 May 2025
Published: 5 June 2025

Citation: Konagaya, M.; Ohsawa, T.; Itoshima, Y.; Kambayashi, M.; Leonard, E.; Tromeur, E.; Misaki, T.; Shintaku, E.; Araki, R.; Hamada, K. Estimation of Wind Conditions in the Offshore Direction Using Multiple Numerical Models and In Situ Observations. *Energies* **2025**, *18*, 3000. https://doi.org/10.3390/en18113000

1. Introduction

Offshore wind power development is expected to progress significantly in Asia, including Japan [1]. Owing to geographical constraints such as water depth, growth in many sea areas begins in coastal regions at shorter distances from the shore (hereafter, nearshore areas) and extends further offshore [2]. Differences in geographical characteristics indicate that wind conditions can vary systematically with distance from shore. Land influences in nearshore areas result in stronger turbulence caused by topographic factors [3]. As one moves further offshore, the impact of land diminishes, and wind conditions evolve owing to the formation of an internal boundary layer. Accurate estimation of wind conditions in nearshore and coastal areas is critical because of the complex and dynamic changes in wind characteristics.

Highly accurate observation and estimation methods are essential for preliminary wind condition surveys of offshore wind farms. Such surveys help secure financing, make investment decisions, and ensure the safe and efficient design of wind turbines. Offshore wind condition surveys typically involve observing local wind conditions using Doppler LiDAR and a meteorological mast, followed by using numerical flow models to estimate wind conditions at turbine heights [4]. In coastal areas with significant land influence, such as Japan, complex wind conditions make it challenging for a single observation point to represent a wind field accurately. Therefore, precise assessment of wind conditions at specific locations and heights for each wind turbine requires a combination of observational data and numerical models. Additionally, quantitative evaluation of the accuracy of these models is vital. This study focused on wind conditions in the offshore direction, where the influence of land is significant near the coast but diminishes further offshore. The accuracy of wind condition estimates in these areas was evaluated using multiple numerical models.

Numerical models commonly used for wind flow estimation include mesoscale meteorological models (hereafter, mesoscale models), computational fluid dynamics (CFD) models, and linear models. Mesoscale models are widely used to describe phenomena spanning wide mesoscale areas. A distinctive feature is their ability to calculate wind flows while solving meteorological variables such as thermodynamics and precipitation. In offshore wind studies, the Weather Research and Forecasting (WRF) model is extensively employed [5], with numerous studies focusing on improving WRF accuracy for seas around Japan [6–9]. In Japan, WRF is also used for developing the NeoWins (NEDO Offshore Wind Information System) offshore wind resource map organized by the New Energy and Industrial Technology Development Organization (NEDO), a Japanese governmental body [10], which aims to maintain the annual average wind speed prediction error within ±5% [11]. However, its bias increases at lower altitudes and near coastlines [12]. Furthermore, its prediction accuracy varies with distance from the shore and whether land influences wind [13].

CFD models are often used for wind condition estimation on land and wake analysis within wind farms because they can reproduce fine-scale phenomena, such as turbulence intensity [14]. In Japan, turbine accidents caused by fatigue from land topography effects have highlighted the importance of considering the turbulence intensity as a critical wind parameter [15], as explicitly stated in Japan's wind farm certification guidelines [16]. Offshore turbulence intensity evaluation has also gained attention [17] owing to the increasing adoption of dual-scanning LiDAR systems in Japan [18]. Linear models with lower computational loads have also exhibited extensive track records. For example, WAsP [19] has been commonly applied to flat terrain and offshore conditions [20]. Recently, CFD capabilities have been integrated into WAsP, enabling its application to complex terrain [21].

The key difference between mesoscale and CFD (or linear) models is their ability to consider thermal phenomena [22]. Mesoscale models incorporate thermal phenomena to predict wind conditions by considering atmospheric stability, significantly affecting the vertical wind-speed profile. By contrast, CFD models typically assume a neutral state. Advanced CFD models capable of accounting for atmospheric stability have been developed and validated using land-based observations [23,24]. The applicability of these models to offshore wind conditions must be validated through direct observations at sea.

Selecting and applying numerical models appropriately in nearshore areas is particularly challenging because of the complex interplay between wind-influencing factors. Therefore, in situ observational data are crucial for validating and comparing models. Konagaya et al. [22] demonstrated that mesoscale models such as sea–land breeze circulation are preferable for regions dominated by thermal phenomena. Although several comparative studies [25–27] have evaluated multiple numerical models, no study has validated wind condition estimates from a coastline several kilometers offshore using dense observational data. This study leveraged a unique dataset obtained through an enhanced offshore wind observation campaign in Japan, in which wind conditions were observed using Doppler LiDAR at four locations from the coast to offshore, enabling the novel validation of numerical models.

This study aimed to estimate nearshore wind conditions using widely applied numerical models and to evaluate their accuracy in both horizontal and vertical directions, with a particular focus on the influence of atmospheric stability. Four numerical models (WRF, MASCOT, WAsP, and Meteodyn WT™) were assessed using multi-point Doppler LiDAR observations conducted from the coast to offshore in northern Japan. The main contributions of this study are:

- ➢ Demonstrating the effectiveness of multi-point LiDAR observations for evaluating wind profiles across coastal and offshore zones.
- ➢ Comparing model performance at hub-height levels under varying atmospheric stability.
- ➢ Clarifying the influence of reference point selection on model accuracy.
- ➢ Providing practical guidance for model application in nearshore wind resource assessments.

Section 2 describes the observational methods and measurement setup. Section 3 outlines the numerical models used in this study and their configurations. Section 4 presents the comparison between the model estimates and observational results. Section 5 discusses the findings, with an emphasis on atmospheric stability and implications for model applicability. Section 6 summarizes the key conclusions of the study.

2. Data and Methods

2.1. Experiment Overview

An offshore wind measurement campaign was conducted as part of an experimental trial project in 2020–2022 for offshore wind measurement technologies, including Floating LiDAR Systems (FLSs) and scanning LiDARs, organized by NEDO [28]. The Mutsu Ogawara site on the Pacific coast of the Aomori Prefecture, Japan, has officially operated as a public testing site since 2024. This site has been extensively used to validate Doppler LiDAR systems, particularly in NEDO projects [18,29,30].

From December 2021 to February 2022, an intensive cross-shore wind observation campaign was conducted at four locations in Mutsu Ogawara Port (Figure 1). The winter period was selected for intensive observation due to the frequent occurrence of strong wind conditions [3], which are representative of high energy yield scenarios and thus suitable for evaluating the performance of numerical models relevant to offshore wind power generation.

At each site, the vertical wind profiles were measured using Doppler LiDAR. Two vertical profiling LiDARs (VLs) were deployed at the coastal site (St.L) and 1.5 km offshore (St.$S_{1.5}$), whereas two FLSs were deployed 3 and 5 km offshore (St.$S_{3.0}$ and St.$S_{5.0}$, respectively) (Figure 2). The primary objective of this campaign was to characterize nearshore wind conditions along the offshore direction.

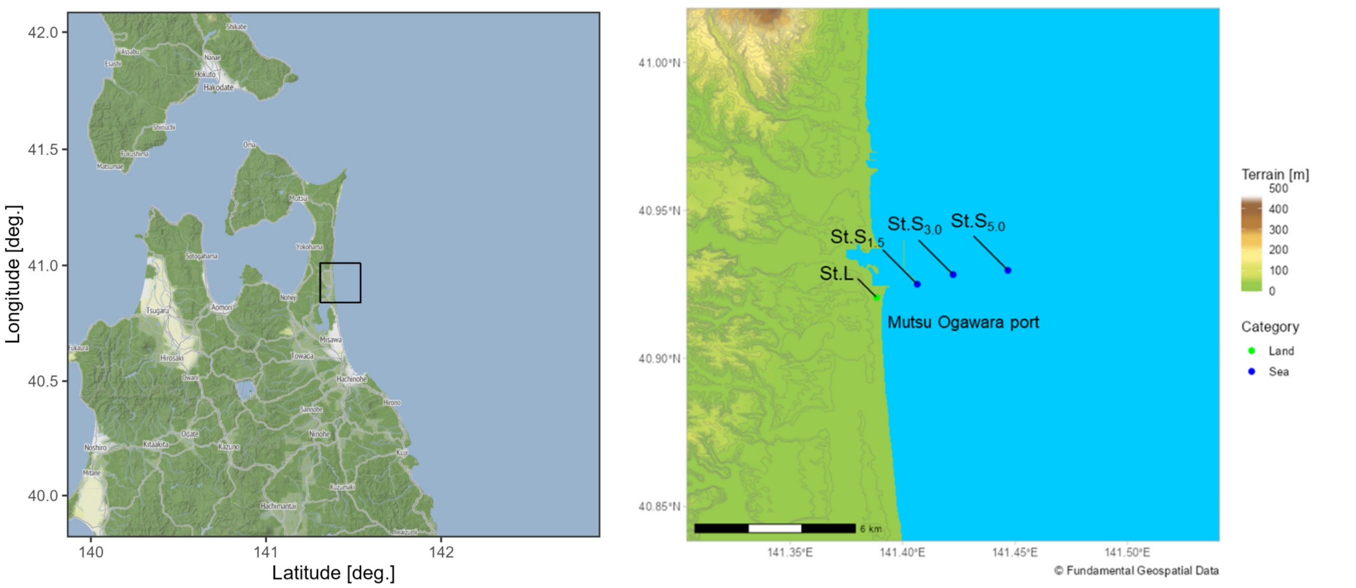

(**a**) (**b**)

Figure 1. Location of the (**a**) North Tohoku area in Japan and (**b**) observation sites around Mutsu Ogawara Port. The black square in (**a**) indicates the area covered in (**b**). Source of (**a**): Konagaya et al. (2021) [3].

Figure 2. Overview of the measurement facilities used in the campaign. The orange solid line runs approximately parallel to the coastline, and the orange dashed line indicates the offshore transect, extending perpendicular to the coastline. Base map source: Google Earth.

The observation site features a north–south-oriented coastline divided into distinct wind sectors: sea-sector wind originating directly from the Pacific Ocean with minimal land influence, and land-sector wind, which, although offshore, is influenced by land conditions [3]. The land-sector wind is a representative case for nearshore areas with residual land effects, evident in the vertical wind speed profiles and turbulence intensity.

For this study, data from all observation points (four observation points × three heights at 63, 120, and 180 m) were analyzed under consistent wind direction conditions: all wind directions (0–360°), sea-sector wind (45–135°), and land-sector wind (225–315°). The analysis was conducted from 15 December 2021 to 28 February 2022 and only used 10 min averaged samples without missing data.

2.2. Observation

2.2.1. Wind Observation

The four observation points were positioned nearly perpendicular to the coastline, which ran in a linear north–south direction. Comparison of these four points enabled analysis of offshore wind condition distribution and provided valuable data for validating the accuracy of the numerical models.

At St.L and St.$S_{1.5}$, wind conditions were observed at 63, 120, and 180 m above the ground or sea level using Vaisala's Windcube V2.1 LiDAR [31]. Offshore, the FLS used at St.$S_{3.0}$ was an AXYS WindSentinel [32] equipped with a Vaisala Windcube V2.0. At St.$S_{5.0}$, a Fugro SEAWATCH [33] equipped with a ZX LiDAR ZX300M [34] was deployed. The wind speed and direction data used in this study were 10 min averaged values obtained from certified Doppler LiDAR systems and are considered sufficiently reliable for model validation. While turbulence intensity estimation using LiDAR remains under development—particularly at higher altitudes—it is recognized as an important subject for future research [35]. Table 1 summarizes the instrument specifications, and Figure 3 illustrates the experimental setup.

Table 1. Summary of the VL and FLS observations.

Site	St.L	St.$S_{1.5}$
VL Model	Windcube V2.1	
Implementer	Vaisala	
Number of observation heights	12	
Observation height from mean sea level [1]	43, 50, 59, **63**, 80, 100, **120**, 140, 160, **180**, 200, and 250 m [2]	50, 59, 80, **63**, 66, 80, 100, **120**, 140, 160, **180**, 200, and 250 m
Measuring range	Speed: 0–55 m/s	
	Direction: 0–360°	
Measuring accuracy	Speed: 0.1 m/s	
	Direction: 2°	
Averaging time	10 min	
Site	St.$S_{3.0}$	St.$S_{5.0}$
FLS model	WindSentinel	SEAWATCH
FLS implementer	AXYS	Fugro
VL model	Windcube V2.0	ZX300M
VL implementer	Vaisala (Leosphere)	ZX LiDAR,
Number of observation heights	12	13
Observation height from mean sea level [1]	43, 50, 59, **63**, 80, 100, **120**, 140, 160, **180**, 200, and 250 m	50, 59, 80, **63**, 66, 80, 100, **120**, 140, 160, **180**, 200, and 250 m
Averaging time	10 min	

[1] Heights used in the analysis are indicated in bold. The heights of the offshore observation points St.$S_{1.5}$, St.$S_{3.0}$, and St.$S_{5.0}$ indicate the mean sea level. [2] The elevation of the land observation point St.L is 7 m, and the heights indicated here are above ground level.

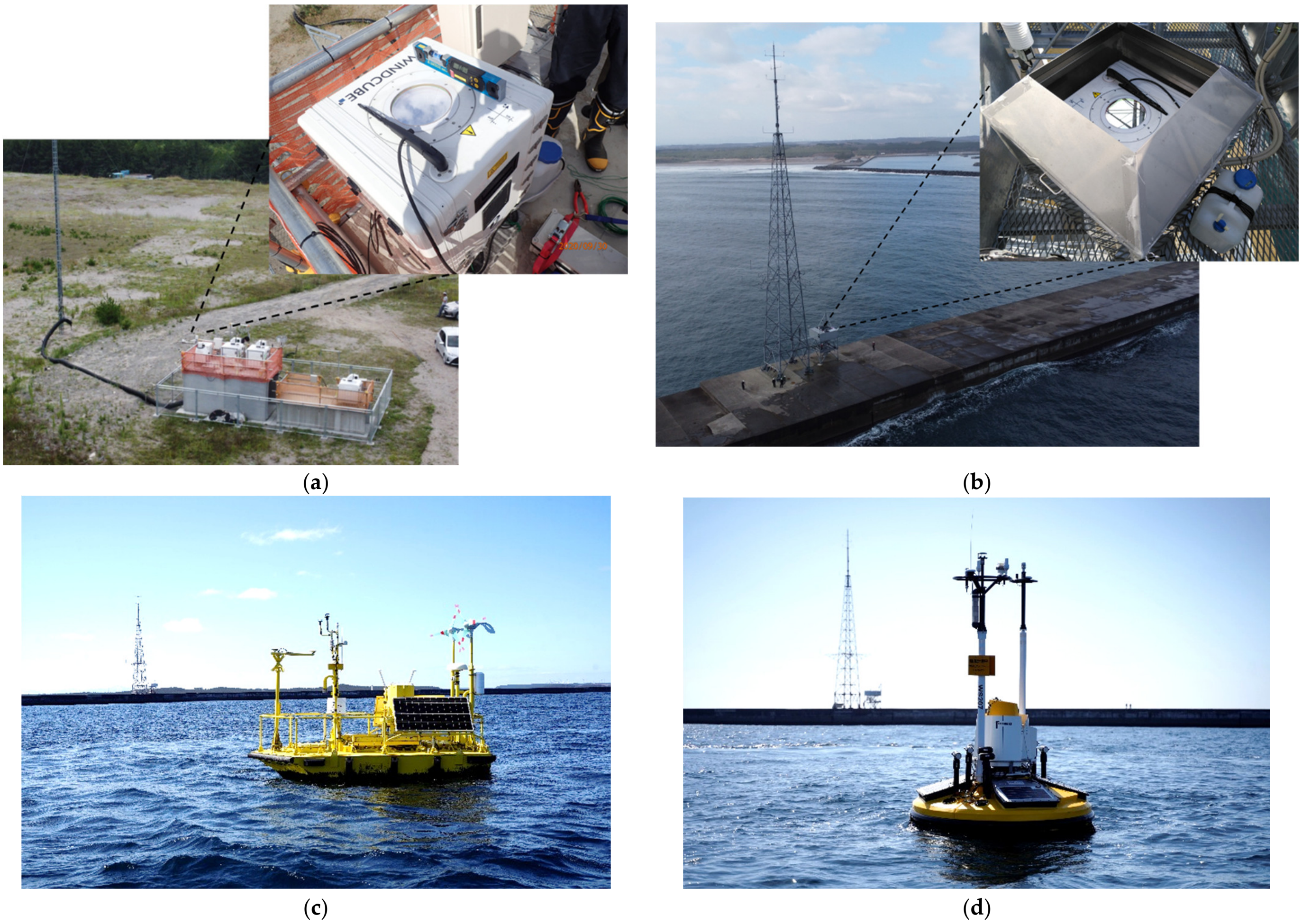

Figure 3. Views of the LiDAR devices used during the observation campaign: (**a**,**b**) VLs in operation during the study period and (**c**,**d**) FLSs during accuracy validation tests conducted before the observation campaign.

Figure 4 shows the accuracy verification results for the LiDAR instruments used in this study. For the onshore (St.L) and nearshore (St.S$_{1.5}$) sites, VLs were calibrated using reference data obtained from the meteorological masts installed within 10 m of each LiDAR station. A comparison was conducted over the entire observation period, allowing for comprehensive evaluation of measurement accuracy.

For the offshore sites (St.S$_{3.0}$ and St.S$_{5.0}$), the FLSs underwent pre-deployment accuracy verification near St.S$_{1.5}$ before starting the main observation campaign. The results demonstrated strong agreement with the reference values, satisfying the best practice criteria established by the Carbon Trust [36], thereby confirming their reliability. Details regarding the specifications and verification procedures for these FLS instruments are provided in our previous publication [30].

To minimize the influence of site-specific environmental factors, only data from the sea sector wind direction (45–135°) were used in the validation analyses for panels (a), (c), and (d). This approach was adopted to reduce the effects of nearby terrain and vegetation (e.g., trees at St.L) or positional differences between the LiDAR and reference instruments. These careful validation efforts ensured that the data used in the subsequent analyses were robust and accurate.

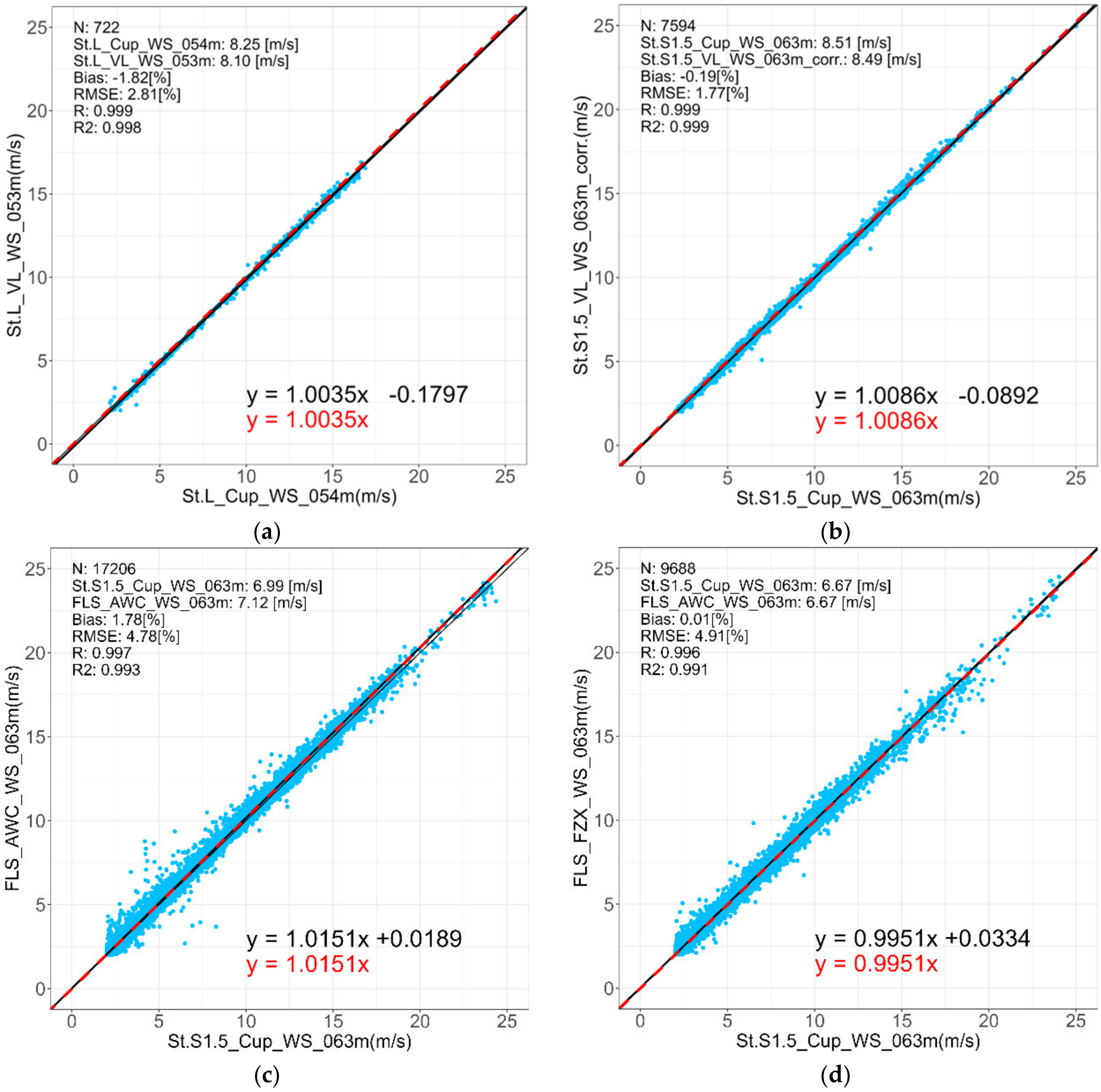

Figure 4. Accuracy verification results of the LiDAR devices used during the observation campaign, compared against reference data from nearby the meteorological masts. The LiDARs installed at each observation point are shown as follows: (**a**) St.L, (**b**) St.$S_{1.5}$, (**c**) St.$S_{3.0}$, and (**d**) St.$S_{5.0}$. The values in the upper left corner of each panel indicate statistics from comparative verification of the two observation data sets.

To ensure data quality, Doppler LiDAR observations were filtered based on data availability rates (≥80%). Only data points with sufficient continuity were retained. The filtered datasets were then used for numerical model validation to ensure robustness and accuracy in the subsequent analyses.

Figure 5 shows the wind speed and direction time series at 120 m at St.$S_{1.5}$ during the study period. Westerly winds, characteristic of the land sector, were predominant, with wind speeds ranging from calm conditions to a peak near 20 m/s.

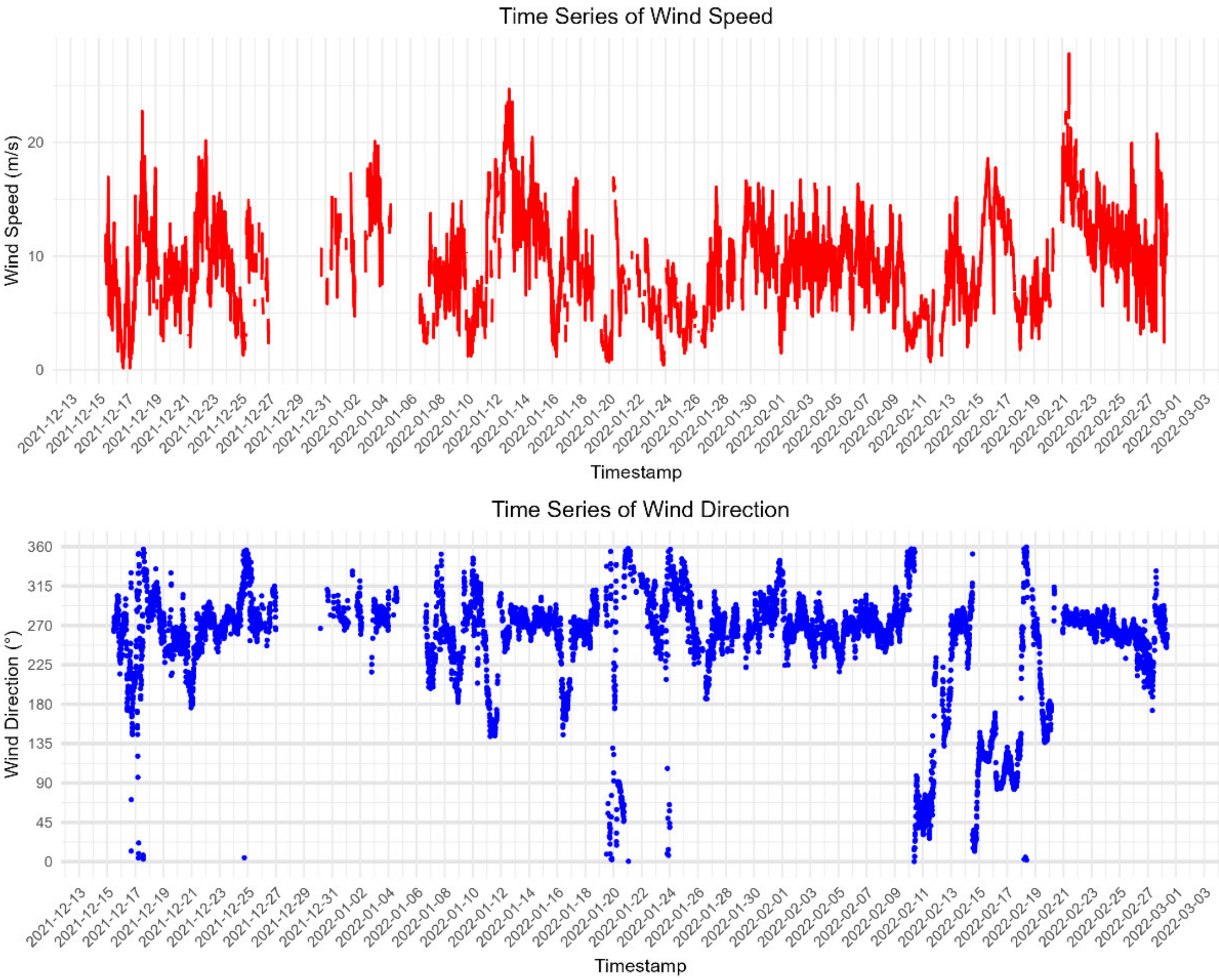

Figure 5. Time series of the 10 min averaged wind speed (**top**) and wind direction (**bottom**) at a height of 120 m at St.$S_{1.5}$ during the study period.

2.2.2. Atmospheric Stability

Atmospheric stability in the surface layer describes the exchange of momentum and heat (latent and sensible) in the vertical direction. This is a key indicator of the likelihood of atmospheric convection and turbulence. Vertical wind shear is closely linked to atmospheric stability, with stronger shear occurring under stable conditions and weaker shear occurring under unstable conditions. This relationship has been validated in previous studies conducted at the Mutsu Ogawara site [3]. In this study, atmospheric stability over land and sea during the observation period was analyzed to assess its thermal effects on the formation of wind conditions.

To evaluate atmospheric stability, which represents the degree of vertical mixing in the atmosphere, the Monin–Obukhov length (MOL) was used as an index to characterize atmospheric stability in the surface layer. In this study, the MOL was calculated at the onshore (St.L) and offshore (St.$S_{1.5}$) sites using the eddy-covariance method, which directly derives the MOL from high-frequency momentum flux and vertical heat flux data. Ultrasonic anemometers were installed 56 m above the ground level at St.L and 61 m above sea level at St.$S_{1.5}$ to ensure a homogeneous horizontal environment. The data obtained from these setups were used for the analysis.

The MOL was derived using the eddy covariance method, and L is defined by Equation (1) [37].

$$L = -\frac{\left(\overline{u'w'}^2 + \overline{v'w'}^2\right)^{3/4}}{\kappa\left(g/\overline{\theta_v}\right)\overline{w'\theta_v{}'}} \quad (1)$$

In this equation, $\overline{u'w'}$ and $\overline{v'w'}$ represent the 10 min mean momentum fluxes in the streamwise and crosswise direction, respectively. The term $\overline{\theta_v}$ is the 10 min mean virtual potential temperature, and $\overline{w'\theta_v{}'}$ is the vertical turbulent heat flux. The constants κ and g denote the von Kármán constant and gravitational acceleration, respectively.

Atmospheric stability was classified into seven categories based on L, as shown in Table 2 [38]. The MOL indicates atmospheric stability, where $L < 0$ represents unstable conditions, $L > 0$ represents stable conditions, and $L \approx \pm\infty$ represents neutral conditions.

Table 2. Atmospheric stability classification by Monin–Obukhov length, L, defined with reference to [38].

L (m)	Atmospheric Stability Category
$-50 < L \leq 0$	Very Unstable
$-200 < L \leq -50$	Unstable
$-500 < L \leq -200$	Near Unstable
$L \leq -500$, $500 \leq L$	Neutral
$200 < L \leq 500$	Near Stable
$50 < L \leq 200$	Stable
$0 < L \leq 50$	Very Stable

3. Numerical Models

This chapter provides detailed information on the four numerical models employed in this study to estimate offshore wind conditions: WRF [5,39–42], MASCOT [5,39–42], WAsP (IBZ [43] and CFD [21]), and Meteodyn WT™ [44]. These models are widely used both in Japan and internationally for wind resource assessment and differ in terms of spatial scale, representation of physical processes and assumptions regarding atmospheric stability. Each of the following subsections provides an overview of the configuration of each model, including aspects such as boundary conditions, grid resolution, and key assumptions.

In this study, all CFD models assume neutral atmospheric stability by default, except for Meteodyn WT™, which accounted for both neutral and unstable conditions. This simplification is common in wind resource assessments, especially with steady-state RANS models. However, it overlooks thermal stratification effects that are often significant in coastal and offshore environments. Ignoring non-neutral stability may lead to inaccuracies in vertical wind shear and turbulence modeling. Recent studies (e.g., Pieterse and Harms, 2013 [45]) highlight the need for improved stability parameterization in CFD evaluations.

The finer spatial resolution of CFD models allows for better representation of mechanical effects such as terrain-induced wind variation, leading to relatively higher accuracy in land-sector wind profile simulations. In contrast, WRF captures large-scale thermodynamic influences but may underrepresent small-scale mechanical features due to its coarser grid.

While model accuracy is the primary focus of this study, it should be noted that the computational requirements of the models vary. Mesoscale models such as WRF generally require high-performance computing resources, whereas commercial CFD models are typically optimized for lower computational load and may run on standard PCs. These differences may influence model selection, depending on the intended application. Among the models evaluated, only WRF is adaptable for mesoscale short-term forecasting, particularly when combined with machine learning. The other models are categorized as diagnostic models and are not intended for direct forecasting use.

3.1. Overview of Models and Reference Settings

Wind conditions are often estimated based on observations at a single location. To reflect this practical approach, we adopted a method in which the data from one observation point served as a reference for estimating the surrounding offshore wind conditions using each numerical model. Specifically, we designated a reference point (Ref) for all the numerical models to provide model input or correction data. In the subsequent analysis, two types of Ref points were used for each numerical model: one located onshore (St.L) and the other located nearshore (St.$S_{1.5}$). The wind speeds at the offshore points (St.$S_{3.0}$ and St.$S_{5.0}$) were estimated based on Refs. A blind method was applied during the numerical model estimations; that is, no observational data from the offshore points (St.$S_{3.0}$ and St.$S_{5.0}$) were excluded from the Ref.

In the mesoscale WRF model, offline corrections were applied to the estimates over time by adding an error vector derived from the difference between the observed values at the Ref and the WRF-calculated values. This correction method, which aligns the model outputs more closely with the observations, has been validated in a previous study [46]. For the other numerical models (MASCOT, WAsP-CFD, WAsP-IBZ, Meteodyn WT™), the observed values at the Ref were directly used as input data.

3.2. WRF

The WRF is a well-established mesoscale model used for weather forecasting and wind resource assessment. One of its key features is the ability to provide a comprehensive range of meteorological parameters. Unlike CFD models, which primarily focus on wind parameters such as speed and direction, mesoscale models also provide additional meteorological elements, including temperature, humidity, and atmospheric radiation.

WRF has a proven track record for generating wind resource maps, such as NeoWins [10]. Unlike CFD models, which require in situ data as input, mesoscale models utilize global or regional objective analysis, which represent meteorological fields for a broader area, as the initial and boundary conditions. In this study, the Local Forecast Model from the Japan Meteorological Agency [47] was used to set the meteorological boundary conditions. The WRF configuration closely followed that used in the NeoWins offshore wind resource map, with updates in the horizontal resolution, land surface roughness length [7], and sea surface temperature (SST) inputs [48] based on recent research findings.

Table 3 and Figure 6 present the configurations and calculation domains of the mesoscale model used in this study. Three-stage nesting was implemented to achieve this resolution, allowing the mesoscale model to cover a much wider calculation domain than other models.

Table 3. Configurations of the Weather Research and Forecasting model, developed with reference to Konagaya et al. (2022) [22].

Model	Advanced Research WRF ver.4.1.2
Period	1 December 2021–31 March 2022 JST
Input data	Met.: Japan Meteorological Agency Local Forecast Model (1-hourly, 0.04° × 0.05° at pressure level and 0.025° × 0.020° at surface level) Soil: NCEP FNL (6-hourly, 1° × 1°) SST: Met Office OSTIA (Daily, 0.05° × 0.05°)
Terrain data	Elevation: METI, NASA ASTER GDEM Land use: MLIT, NLNI land use subdivision mesh
Grids	Domain 1: 2.5 km × 2.5 km (100 × 100 grids) Domain 2: 0.5 km × 0.5 km (100 × 100 grids) Domain 3: 0.1 km × 0.1 km (130 × 150 grids)
Vertical levels	40 layers (surface to 100 hPa)
Physics options	Shortwave process: Dudhia scheme Longwave process: Rapid Radiative Transfer Model scheme Cloud microphysics process: Ferrier (new Eta) scheme PBL process: Mellor–Yamada–Janic (Eta operational) scheme Surface layer process: Monin–Obukhov (Janic Eta) scheme Land-surface process: Noah Land Surface Model scheme Cumulus parameterization: Kain–Fritsch (new Eta) scheme (Domain 1)
FDDA	Domain 1: Enabled (U, V, T, Q) Domain 2, 3: Enabled (U, V, T, Q), excluding the interior of PBL

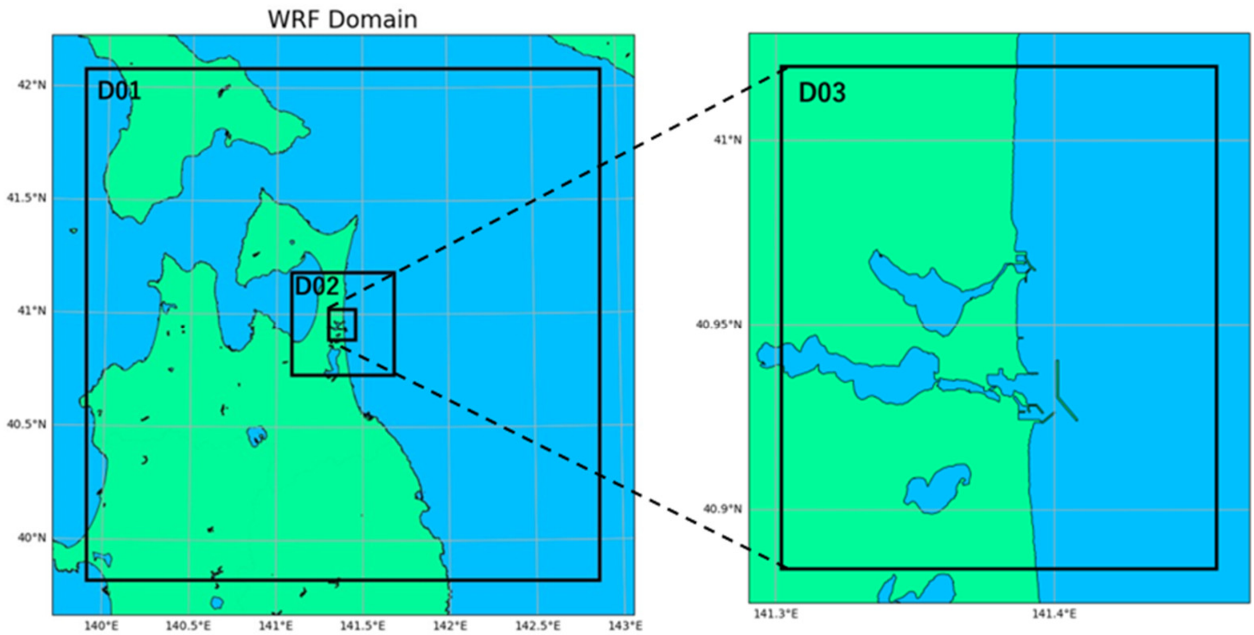

Figure 6. Calculation domains 1–3 of the Weather Research and Forecasting model (WRF). Domains as provided in Table 3.

3.3. MASCOT

MASCOT, a nonlinear CFD model based on the Reynolds-averaged Navier–Stokes (RANS) method, is extensively used for onshore wind resource assessments in Japan owing to its strong performance in simulating high-resolution wind fields over complex terrain. This forms the technical foundation for certifying onshore and offshore wind power facilities in Japan [16]. In MASCOT, neutral wind conditions are simulated based on the terrain and roughness length within the calculation domain. Wind calculations rely on the wind speed for each direction relative to the Ref, making accurate estimations of wind speed ratios and direction differences crucial.

The configurations and calculation domains of MASCOT are listed in Table 4 and illustrated in Figure 7a. Terrain data were derived from the 50 m digital elevation model [49] published by the Geographical Survey Institute. At the same time, roughness length information was generated using land use data provided by the Ministry of Land, Infrastructure, Transport, and Tourism [50] (Table 5). These configurations represent the default settings for the MASCOT analysis. The terrain distribution (Figure 7a) and roughness length map (Figure 7b) show that forested areas in complex terrain were prevalent across the land portion of the domain.

Table 4. Configurations of MASCOT. Elevation data provided by the Geospatial Information Authority of Japan (GSI) [49].

Model	MASCOT Ver.5.1a
Center of the calculation domain	40° 55′ 3.25″ N, 141° 23′ 32.68″ E (Tokyo Datum)
Elevation data	GSI 50 m grid digital elevation model data
Ground roughness	Based on the 100 m mesh land use data
Size of the calculation domain	18 km × 18 km
Wind direction	16 directions
Minimum horizontal resolution	25 m
Minimum vertical resolution	5 m
Calculation domain as minimum resolution	Within a 7000 m radius
Number of mesh	29,261,232

Table 5. Default roughness length values for various land use types in MASCOT.

Type	Roughness Length (m)
Rice field (Tanbo)	0.03
Field	0.1
Orchard	0.2
Other wood field	0.1
Forests	0.8
Wasteland	0.03
High buildings	1
Low buildings	0.4
Transportation area	0.1
Other area	0.03
Lakes and ponds	0.0002
River A: Does not include artificial land use in river areas	0.001
River B: Artificial land use in riverbeds	0.001
Beach	0.03
Sea	0.0002

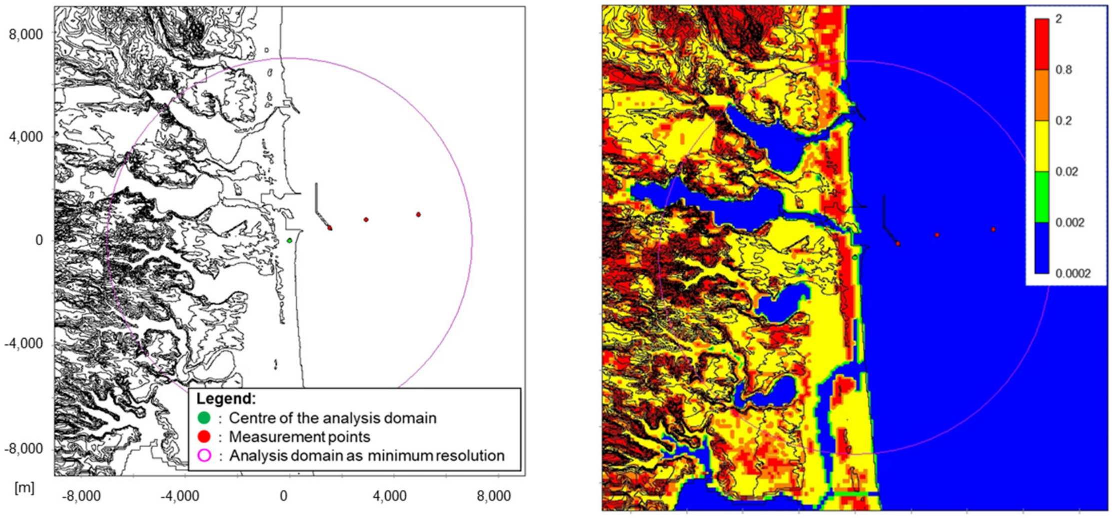

(**a**) (**b**)

Figure 7. (**a**) Calculation domain and (**b**) roughness length of MASCOT.

3.4. WAsP (WAsP-IBZ, WAsP-CFD)

WAsP is a commonly used industry-standard software program developed by the Technical University of Denmark for wind resource assessment, turbine siting, and energy yield calculations for wind turbines and wind farms. It incorporates several physical models to simulate wind climate and flow over varying terrains and near obstacles. For horizontal and vertical extrapolation of wind flow, WAsP uses the built-in linear IBZ model, which performs well on flat to moderately complex terrain. For more complex terrain with steep slopes, a CFD model is also available for calculations in the WAsP [43].

This study uses both WAsP-IBZ [43] and WAsP-CFD [21]. The configurations and calculation domains of the WAsP models are listed in Tables 6 and 7. In the far-field regions illustrated in Figure 8, the terrain was filtered and smoothed to reduce the complexity before generating the computational grid. All calculations were performed using WindPRO version 3.6.366, developed by EMD International [51]. The PARK module used in this study was part of this WindPRO version. We used a model integrated into the PARK software module for WAsP-IBZ. For WAsP-CFD, a rectangular domain of 2 km was configured to cover the relevant area, and the calculation results were obtained.

Table 6. Configurations of WAsP-IBZ.

Model	WAsP-IBZ (WAsP Version 12)
Azimuth resolution in BZ model	5°
Decay length for roughness area size	10,000 m
Default background roughness area size	0.03 m
Height of inversion in BZ model	1000 m
Max. interpolation radius in BZ model	20,000 m
Max number of roughness changes/sector	10
Max. rms error in log(roughness) analysis	0.3
Softness of inversion in BZ model	1
Sub-sectors in roughness map analysis	9
Width of coastal zone	10,000 m
Wind direction	16 directions

Table 7. Configurations of WAsP-CFD.

Model	WAsP-CFD Version: 1.11.2.7
Number of calculation domain	Four tile domains
Size of calculation domain	4 km × 4 km in each domain
Calculation domain as minimum resolution	2 km × 2 km in each domain
Wind direction	36 directions
Mean resolution horizontal/vertical	20.7/5 m
Domain height/diameter	14/34 km

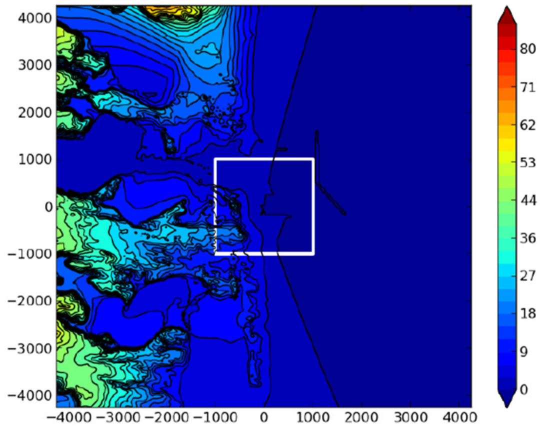

(**a**) Onshore domain near St.L

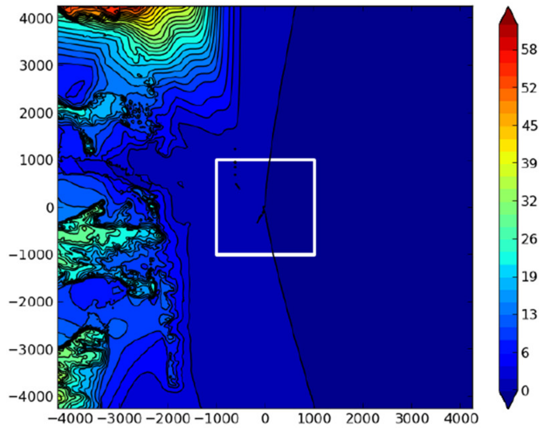

(**b**) Nearshore domain near St.$S_{1.5}$,

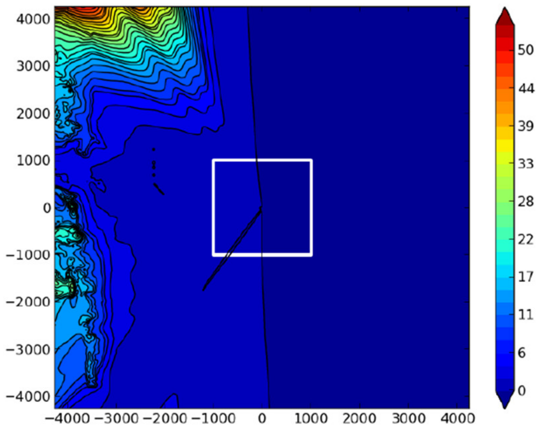

(**c**) Offshore domain near St.$S_{3.0}$,

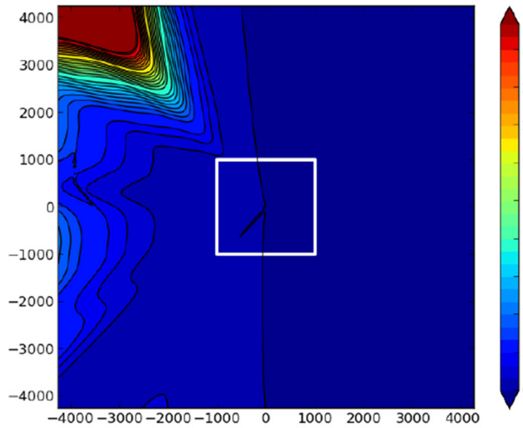

(**d**) Offshore domain near St. $S_{5.0}$.

Figure 8. Calculation domains of WAsP-CFD, spanning from (**a**) land to (**d**) sea. Each panel depicts the terrain prepared for computational fluid dynamics (CFD) calculations, with the white square representing the detailed calculation domain. Note that the elevation legend differs for each figure panel.

3.5. Meteodyn WT™ (Neutral, Unstable Condition)

Meteodyn WT™ is a widely used commercial CFD application for wind resource assessment. It is based on the RANS method and solves three-dimensional momentum and mass conservation equations to estimate the 3D wind speed vector [52]. Table 8 presents the calculation configurations, and Figure 9 shows the topography and roughness length map used in Meteodyn WT™.

Table 8. Configurations of Meteodyn WT™.

Model	Meteodyn WT™ Version: 1.9
Center of the calculation domain	40°55′29.4″ N, 141°25′5.6″ E (WGS84)
Site radius	13 km
Elevation data	Nasadem: 30 m resolution
Roughness data	Copernicus, 2019 [53] 100 m resolution
CFD minimum horizontal resolution	25 m
CFD minimum vertical resolution	4 m
Number of directions	20
Number of cells in the mesh	Direction 90 deg: 4,046,112 Direction 270 deg: 3,933,720

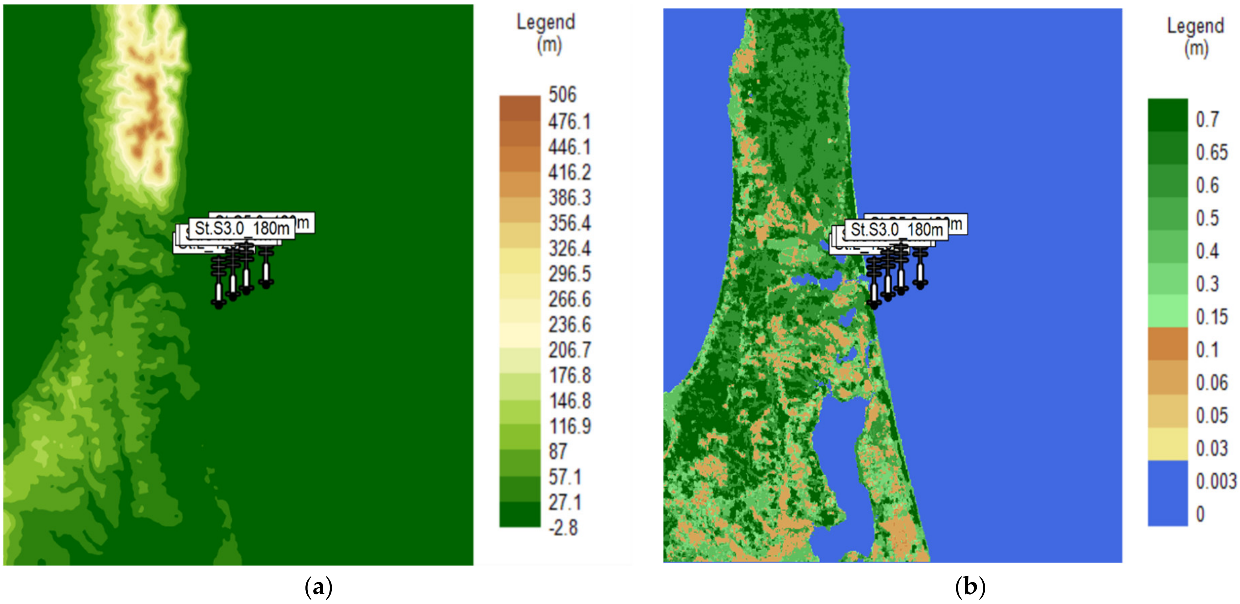

Figure 9. (**a**) Topographic domain and (**b**) roughness length of Meteodyn WT™.

Meteodyn WT™ is unique among CFD models because it can consider topography and roughness length while assuming a specific atmospheric stability. This hybrid capability allows it to account for detailed terrain considerations similar to CFD models and thermally driven atmospheric stability similar to mesoscale models. However, the Meteodyn WT™ model used in this study assumes constant atmospheric stability rather than time-varying atmospheric stability, distinguishing it from typical mesoscale models.

Atmospheric stability conditions were determined using the wind profile calibration method for each land and sea wind sector (Figure 10) [54]. The vertical wind profiles observed at St.L were compared for calibration. The model incorporates an unstable condition that best matches the observed vertical profile in the sea sector. Forest calibration was adopted for the land sector under neutral thermal stability conditions owing to the highly forested environment. This calibration adjusted the software parameters to align the simulated wind profile with the observed measurements using wind speed profile data to adapt the CFD forest model to actual forest properties.

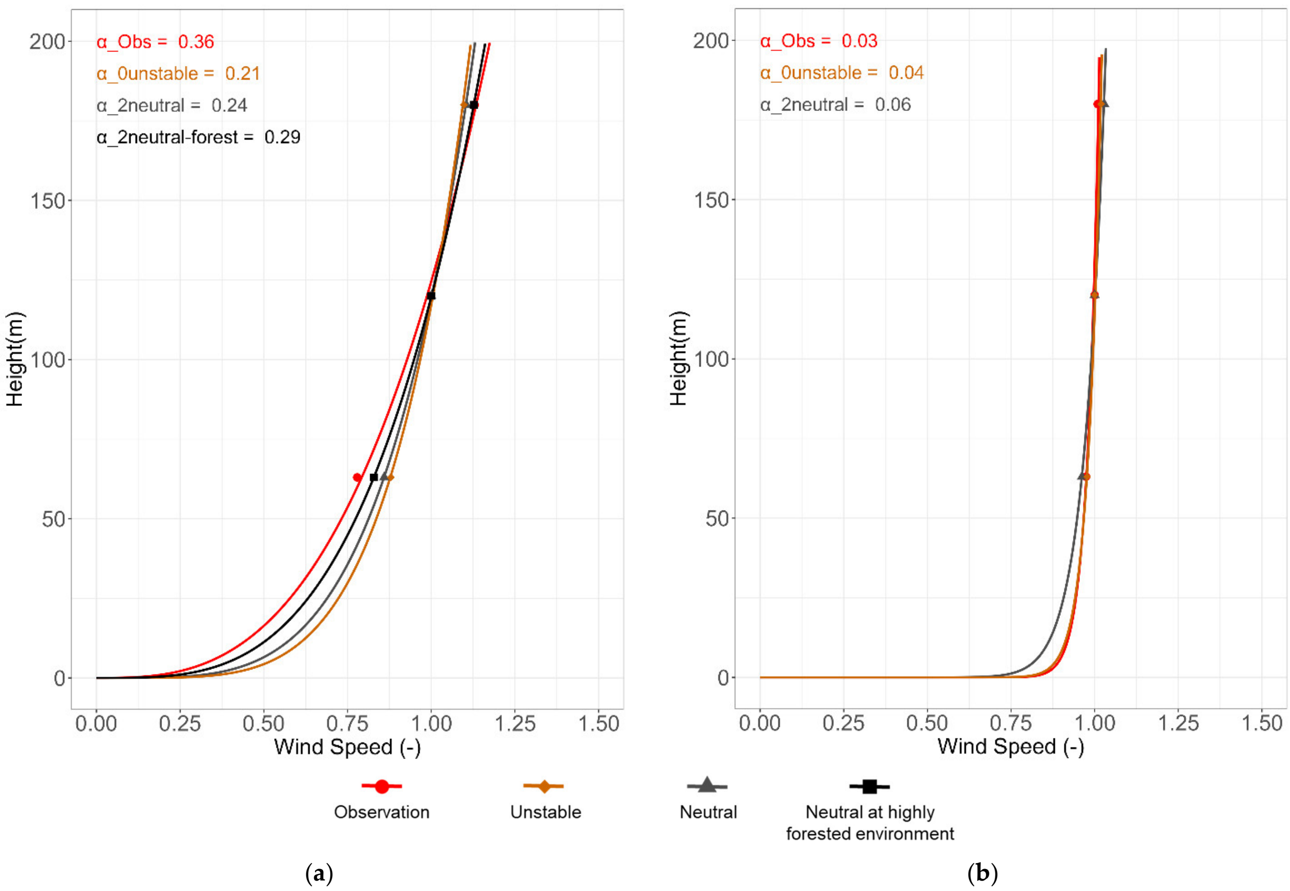

Figure 10. Stability calibration of Meteodyn WT™ at (**a**) land and (**b**) sea wind sectors. The numerical values shown in the upper left corner of each panel represent the power-law exponent (α), which indicates the magnitude of vertical wind shear.

In Meteodyn WT™, the forest model is described by the following parameters:

- ➢ Tree height was defined by roughness length values and the ratio (R) between tree height and roughness length (default R = 20).
- ➢ Forest density directly affects the drag force term from forest effects (default: normal forest density) [52].

4. Results

4.1. Observed Wind Conditions

The wind direction characteristics observed at the study sites during the study period are shown in Figure 11. The primary wind directions at three heights (63, 120, and 180 m) at the land-based site St.L and the offshore sites St.$S_{1.5}$, St.$S_{3.0}$, and St.$S_{5.0}$ (Figure 11) predominantly showed westerly winds from the land sector, with minimal variation across locations and heights. Wind speeds by direction indicated higher wind speeds in the land sector; however, the easterly winds from the sea sector reached approximately 20 m/s. The average wind speeds were higher for easterly and westerly winds than in other directions, clearly reflecting a wind axis nearly perpendicular to the north–south coastline.

The period-averaged wind speeds at three heights (63, 120, and 180 m) at the four sites are shown in Figure 12. The vertical wind shear between the land- and sea-sector winds exhibited significant differences, highlighting their distinct directional characteristics.

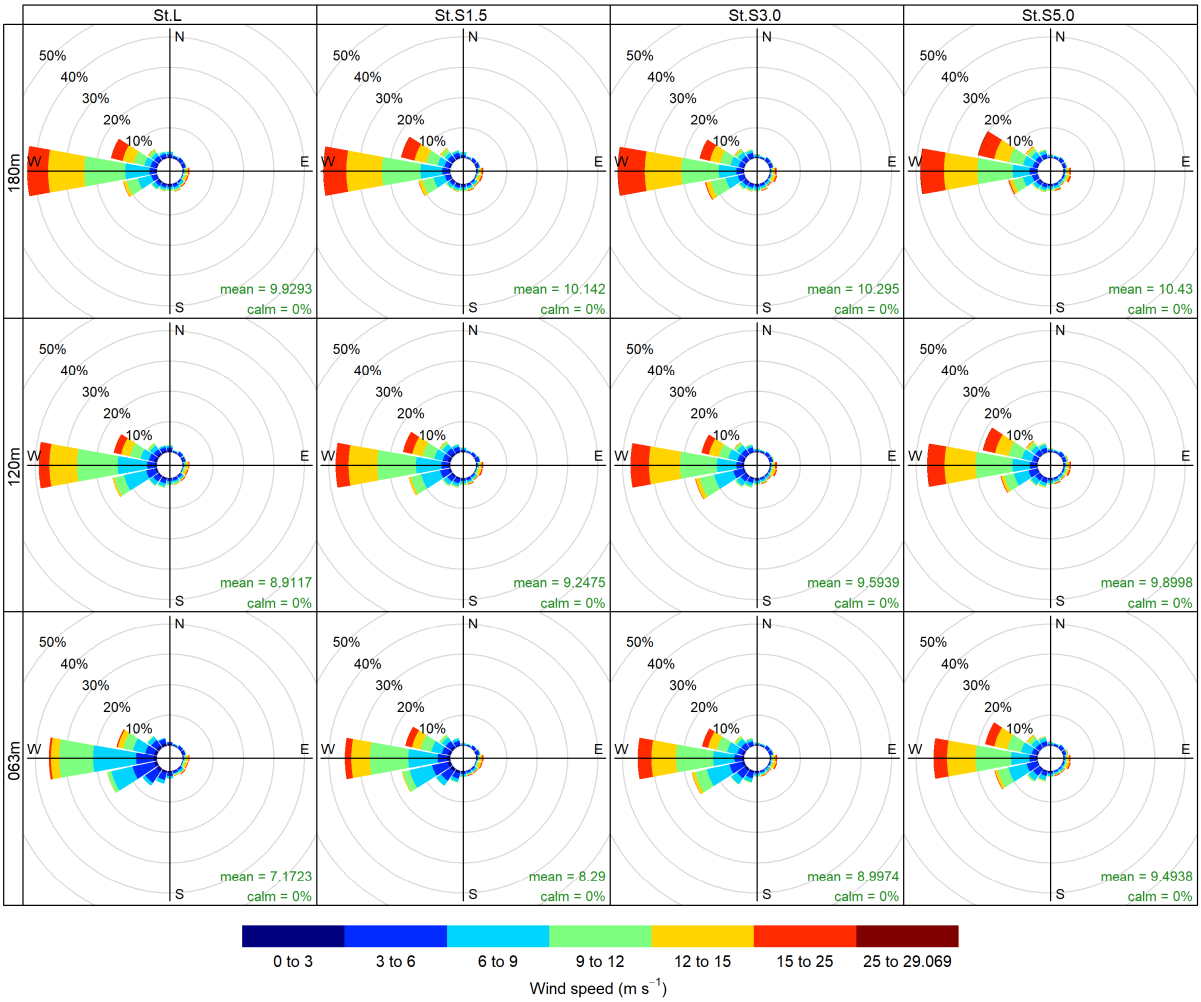

Figure 11. Wind rose diagrams showing observed wind characteristics during the study period at all four sites (St.L, St.S$_{1.5}$, St.S$_{3.0}$, and St.S$_{5.0}$). The values in the lower right corner of each panel indicate the mean wind speed and frequency of calm periods, respectively.

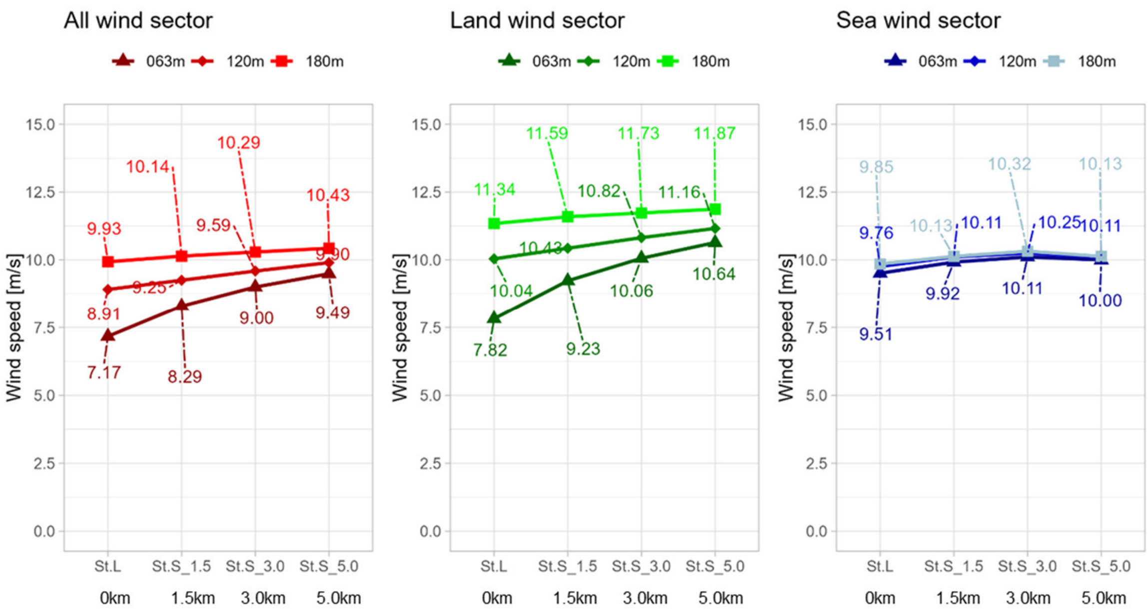

Figure 12. Distribution of period-mean wind speed observations for (**left**) all wind directions, (**middle**) land-sector wind, and (**right**) sea-sector wind by height in the offshore direction.

Focusing on land-sector winds, wind speeds in the lower layers decreased sharply near the coast, resulting in substantial vertical wind shear. This indicates the influence of the terrain and other land-based factors. As these winds move offshore, the wind speeds in the lower layers rapidly recover, and the vertical shear diminishes. However, even 5 km offshore, the vertical shear of the land-sector winds remained larger than that of the sea-sector winds, indicating a lingering land influence. Conversely, the sea-sector winds showed minimal horizontal and vertical variations from the coast to offshore, exhibiting a nearly uniform distribution. A slight decrease in wind speed near the coastline was observed, likely owing to the blockage effects caused by land.

4.2. Observed Atmospheric Stability

The occurrence frequencies of the atmospheric stability classes derived from the observed data are shown in Figure 13. During the study period, unstable stratification (near-unstable, unstable, and very unstable) was observed over the sea more than 70% of the time. This is attributed to the SST being warmer than the air temperature in winter, with the sea acting as a relative heat source. Over land, neutral conditions were observed approximately 50% of the time, and when stable conditions (near-stable, stable, and very stable) were included, the frequency reached approximately 80%. This was likely because of the dominant westerly winds from the land sector during winter, combined with snow cover cooling the near-surface air, creating neutral to stable atmospheric conditions.

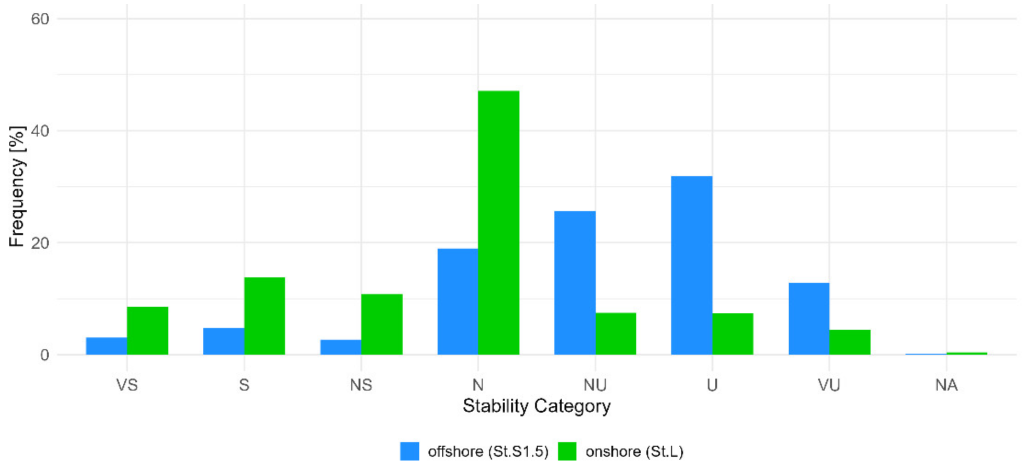

Figure 13. Atmospheric stability occurrence rates over land and sea during the study period (15 December 2021–28 February 2022). The stability categories are abbreviated as follows: VS = Very Stable, S = Stable, NS = Near Stable, N = Neutral, NU = Near Unstable, U = Unstable, VU = Very Unstable, NA = Not Available.

Figure 14 illustrates the hourly occurrence frequencies of atmospheric stability at the onshore observation site St.L and the offshore site St.$S_{1.5}$, divided into warm and cold seasons. Focusing on hourly variations, unstable land conditions increased in frequency during the day owing to convection driven by solar radiation, whereas the opposite trend was observed at night. This trend was observed on land during both the cold and warm seasons.

In contrast, the hourly offshore variations were less pronounced than the onshore variations. However, during the cold season, a diurnal cycle was also evident offshore, with unstable conditions occurring more frequently during the daytime. This is primarily because the SST is warmer than the air advected from land, leading to generally unstable atmospheric conditions over the sea [3]. At night, a slight increase in the frequency of stable conditions offshore was observed, likely owing to the advection of a stable layer that had developed over the land.

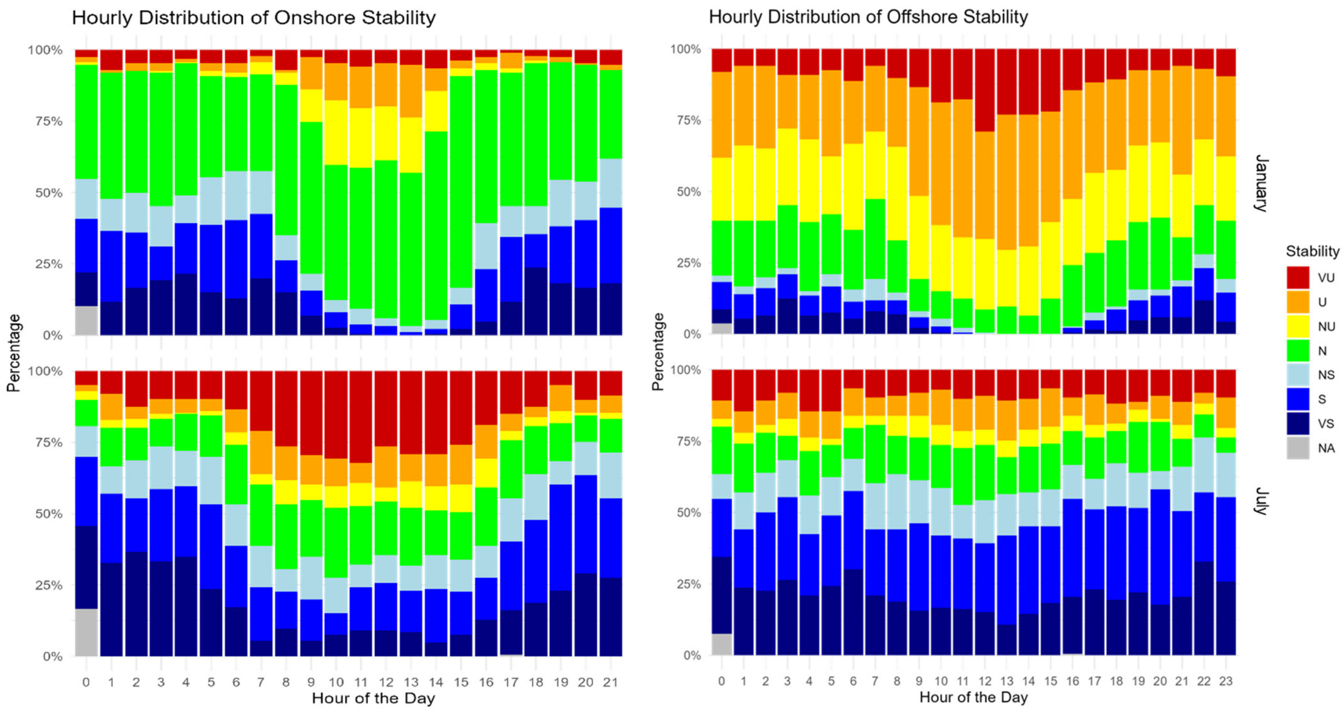

(**a**) (**b**)

Figure 14. Monthly diurnal variations in atmospheric stability over the (**a**) land and (**b**) sea. The upper panels show results for the cold season (January 2022), and the lower panels show the warm season (July 2022).

During the warm season, no significant hourly variations were observed offshore, and a general tendency toward stabilization was evident. This can be attributed to the increased frequency of sea sector winds, which reduce the influence of land.

4.3. Model Analysis

This subsection compares the estimates of each numerical model with the observational data presented in the previous subsection. Figure 15 shows a conceptual diagram of the accuracy validation process. Each numerical model uses observational data from a Ref to estimate the mean wind speeds at various locations and heights during the study period.

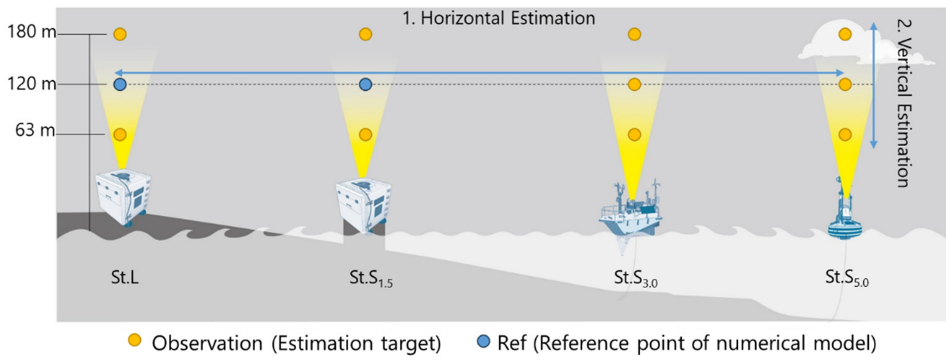

Figure 15. Conceptual diagram of numerical model accuracy estimation and observation points.

The accuracy validation was performed in two steps:

1. Horizontal Estimation: Assessment of the estimation accuracy in the horizontal offshore direction at the same height (120 m) as the Ref.
2. Vertical Estimation: Evaluation of the estimation accuracy in the vertical direction, including heights different from the Ref (63 and 180 m).

The accuracy and reliability of the models in estimating offshore wind conditions can be quantitatively evaluated by comparing the numerical model estimates to the in situ data at these designated points and heights.

4.3.1. Horizontal Estimation Accuracy

First, we examined the accuracy of horizontal estimation. Figure 16 illustrates the horizontal distribution of the mean wind-speed bias estimated by each numerical model during the analysis period. Two types of Refs were used; results using the onshore St.L as the Ref are shown in the left part of Figure 16, and those using the nearshore St.$S_{1.5}$ (approximately 1.5 km offshore) as the Ref are presented in the right part. In both cases, the numerical models referenced the values observed at a height of 120 m for estimation.

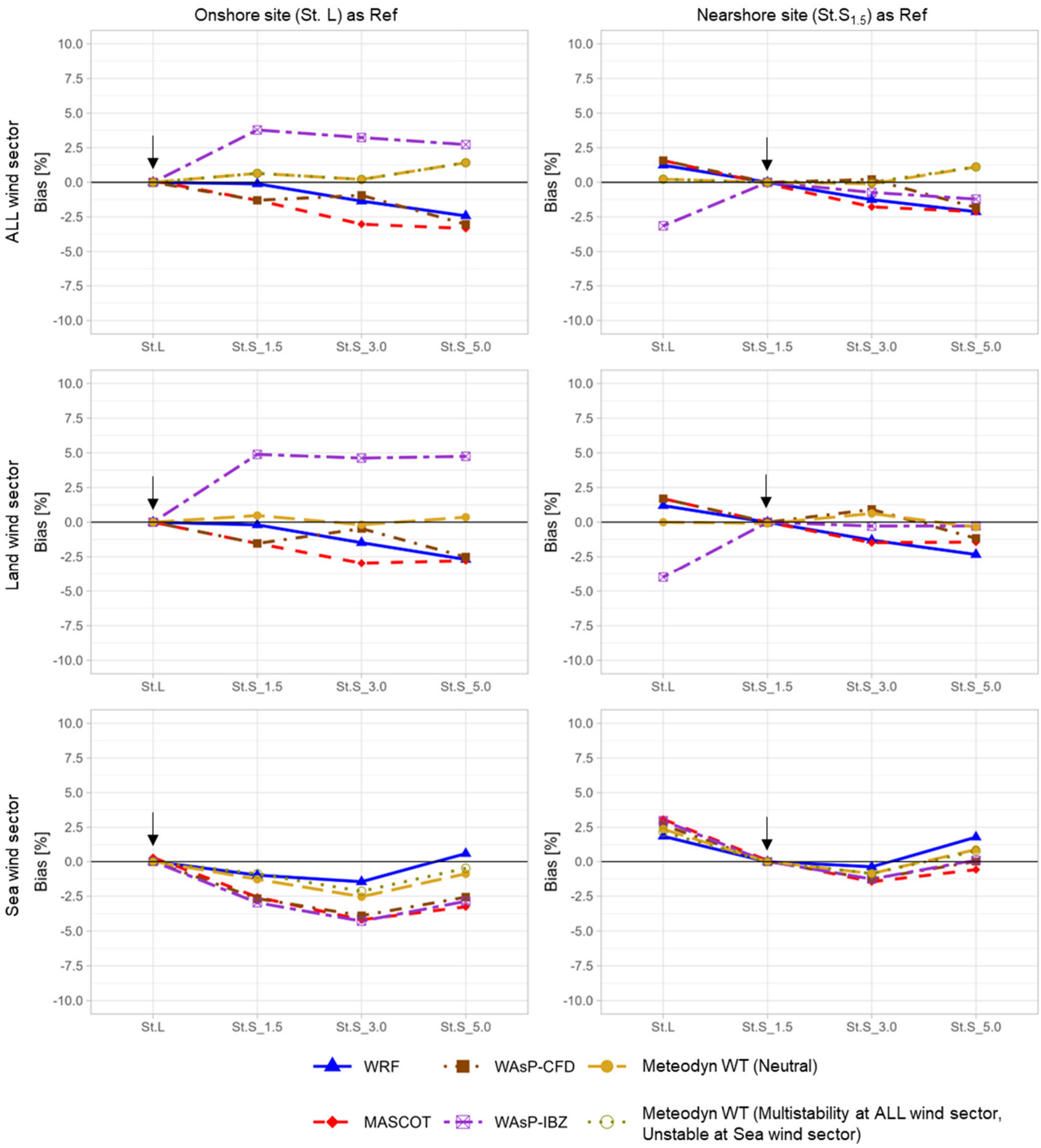

Figure 16. Horizontal bias distribution (%) in mean wind speed estimates at a 120 m height for each numerical model. Arrows indicate the reference point (Ref) used for model input or correction. The left panel shows where the Ref is set at the onshore site (St.L), and the right panel at the nearshore site (St.$S_{1.5}$).

Comparing the two references, using nearshore St.S$_{1.5}$ as the Ref yielded higher accuracy across all numerical models, regardless of the wind direction sector. This configuration ensured that biases in the estimated wind speeds for offshore locations, such as St.S$_{3.0}$ and St.S$_{5.0}$, were within $\pm$2.5%. These results suggest that offshore observations from St.S$_{1.5}$, even at a distance of just 1.5 km from the coast, are more effective for accurately assessing offshore wind conditions than onshore observations from St.L. Specifically, the use of scanning LiDAR and FLS for offshore wind observations can significantly enhance the accuracy of wind estimates in nearby seas and offshore areas.

When using the coastal St.L as the Ref, the estimation accuracy notably decreased as the distance offshore increased. This reduction in accuracy is likely because of the diminishing representativeness of the observational data with increasing distance from the Ref. For land-sector winds, the three numerical models (WRF, MASCOT, and WAsP-CFD) showed a negative bias in their estimates as the offshore distance increased, indicating that the horizontal wind speed gradient was slightly underestimated compared to the observed values. Conversely, WAsP-IBZ overestimates the horizontal wind speed gradient in the nearshore area, which is consistent with the findings of Jimenez et al. (2007) [25]. Among all models, Meteodyn WT™, which assumes neutral conditions, exhibited the highest accuracy in estimating land-sector winds, likely owing to the significant effect of forest calibration at St.L.

When St.L was used as the Ref for sea-sector winds, nearly all the numerical models showed a negative bias in their estimates as the offshore distance increased. However, the models that most accurately reproduced the wind conditions were the WRF and Multi-stability Meteodyn WT™ (considering unstable conditions), which accounted for atmospheric stability.

4.3.2. Vertical Estimation Accuracy

We then focused on vertical wind shear in the numerical estimation models. Figure 17 presents the vertical profiles of the mean wind speed estimates from each numerical model. The calculation results using the 120 m height at St.S$_{1.5}$ as the Ref were used to fit a vertical profile based on the power law to the wind speed values at three different heights at each location.

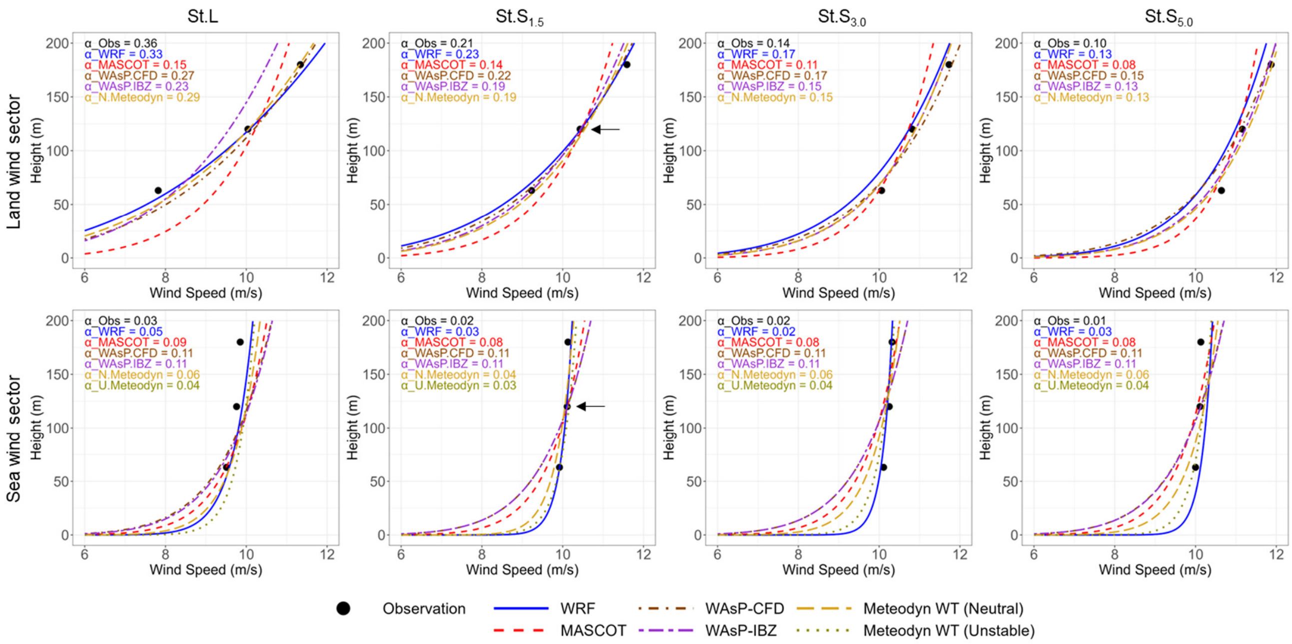

Figure 17. Vertical wind profiles of observed and estimated mean wind speeds from the numerical models. The Ref for all numerical models is consistently set at 120 m above St.S$_{1.5}$, as indicated by the arrows. The numerical values shown in the upper left corner of each panel represent the power law exponent (α), which quantifies the magnitude of vertical wind shear.

Figure 17 also displays the fitted power law exponent (α), which represents the magnitude of vertical wind shear. Similar to the observations shown in Figure 12, the vertical wind shear represented by each numerical model exhibited different trends for land- and sea-sector winds. For land-sector winds, the observed power law exponent α decreased from the coast (St.L) to offshore (St.$S_{5.0}$) (0.36 to 0.10), and a similar trend of decreasing α values with increasing distance offshore was observed in the estimates from each numerical model. However, differences are noted in the absolute values of α among the models. Comparing the average values for the two offshore locations, St.$S_{3.0}$ and St.$S_{5.0}$, MASCOT (0.10) underestimated the observed value (0.12), whereas WRF (0.15), WAsP-CFD (0.16), WAsP-IBZ (0.14), and Neutral Meteodyn WT™ (0.14) tended to overestimate the vertical wind shear.

5. Discussion

5.1. Wind Characteristics and Influencing Mechanisms

Wind characteristics in coastal areas represent a major source of uncertainty in numerical-model-based wind estimations. In the study area, wind behavior differs between land-sector winds, which are influenced by terrain and land features, and sea-sector winds, which are predominantly governed by atmospheric thermodynamic conditions.

Sea-sector winds are not considerably influenced by mechanical factors such as topography and rely more heavily on thermodynamic factors. The high accuracy of vertical shear reproduction by the WRF and Unstable Meteodyn WT™ can be attributed to their ability to incorporate the effects of unstable atmospheric stratification during the study period (Figure 18). For Meteodyn WT™, comparison of configurations with different atmospheric stability assumptions revealed better estimation accuracy under unstable conditions. The average α value for the two offshore sites under unstable conditions was 0.04, closer to the observed value of 0.02, compared with 0.06 under neutral conditions. This underscores the importance of considering atmospheric stability when predicting offshore wind conditions.

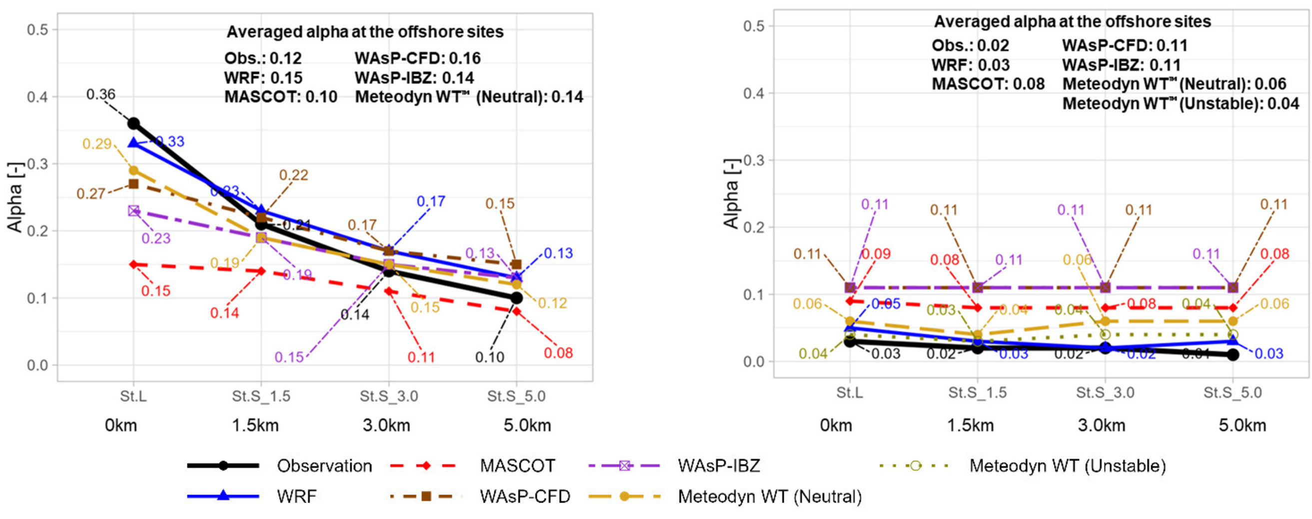

(**a**) (**b**)

Figure 18. Power law exponent (α) of the wind speed profile derived from observations and numerical models: (**a**) land-sector wind and (**b**) sea-sector wind. The numerical values in the upper right corner of each panel represent the average α value at two offshore sites (St.$S_{3.0}$, St.$S_{5.0}$).

For land-sector winds, the influence of topography was observed up to 5 km offshore (Figure 12), emphasizing the significance of mechanical factors, such as the roughness of the transition from land to sea. The mechanical effects on wind are expected to diminish with increasing distance from the coastline (Figure 18a), eventually resembling sea-sector wind characteristics further offshore (Figure 18b). During the study period, atmospheric stability over land was predominantly neutral (Figure 13), and land-sector winds were strongly affected by topography and windbreak forests. Consequently, the benefits of the numerical models that account for atmospheric stability (WRF and Unstable Meteodyn WT™) were not particularly evident for land-sector winds.

However, unlike the neutral conditions over land, offshore areas were dominated by unstable stratification. This led to an overestimation of vertical shear (α) values at offshore sites (St.$S_{3.0}$, St.$S_{5.0}$) by the numerical models. This overestimation suggests that the unstable sea surface thermally influences land-sector winds as they pass over it. Therefore, numerical models that incorporate atmospheric stability considerations similar to those used for sea sector winds are recommended even in coastal areas affected by land.

5.2. Spatial and Temporal Variation of Atmospheric Stability

To what extent can the atmospheric stability frequencies observed during the study period, specifically neutral conditions over land and unstable conditions offshore (Figure 13), be considered a universal phenomenon? This question concerns the reproducibility of calculating atmospheric stability using numerical models. Among the numerical models used in this study, the CFD models (MASCOT, WAsP-CFD, and Meteodyn WT™) and linear model (WAsP-IBZ) were calculated based on uniform atmospheric stability assumptions across spatial and temporal dimensions. These models assumed only neutral conditions, except for Meteodyn WT™, which accounts for non-neutral atmospheric stability. If atmospheric stability varies significantly in space and time, particularly when deviating from neutrality, the accuracy of these models may decrease compared to the results obtained in this study.

As shown in Section 4.2 and Figure 14, atmospheric stability in coastal areas varies spatiotemporally with frequent non-neutral conditions. Particularly during the warm and cold seasons, significant temperature differences between land and sea surfaces result in atmospheric layers with distinct stability forming within a mere 1.5 km between St.L and St.$S_{1.5}$. To accurately estimate wind conditions, spatiotemporal variations in atmospheric stability must be accounted for within numerical models, as failure to consider them may reduce the accuracy of reproducing vertical wind speed profiles (Figure 18).

Mesoscale models that can incorporate the thermal conditions at each grid point over time are advantageous for capturing these variations. This advantage is reflected in the consistently high estimation accuracy of WRF in the coastal-to-offshore direction (Figure 18). However, the model tends to slightly underestimate the rate of wind speed increase for land-sector winds blowing offshore, suggesting that further improvements are needed to address dynamic factors such as surface roughness in nearshore areas [7].

Conversely, while CFD models exhibit high reproducibility at the microscale, they struggle to account for spatiotemporal variations in atmospheric stability because of their inherent limitations. Therefore, an integrated approach combining mesoscale and microscale modeling is necessary for accurate nearshore and offshore wind estimations. For instance, incorporating the output from mesoscale models, global or regional objective analysis as boundary conditions, and volume forcing for CFD model calculations could provide an effective solution.

6. Conclusions

This study evaluated the accuracy of four numerical models (WRF, MASCOT, WAsP and Meteodyn WT™) for estimating nearshore offshore wind conditions at Mutsu Ogawara Port, using multi-point Doppler LiDAR observations. The key findings are summarized as follows:

1. Horizontal Estimation: Wind speed estimation accuracy in the offshore direction improved when using a nearshore reference (St.S$_{1.5}$) instead of an onshore reference (St.L). Biases in the offshore area were generally within ±2.2% up to 5 km from the coast, indicating the practical advantage of using nearshore measurement locations.
2. Vertical Estimation: Models incorporating atmospheric stability (e.g., WRF, Meteodyn WT™ under unstable conditions) better reproduced vertical wind profiles offshore. In contrast, models assuming neutral stability tended to overestimate wind shear, particularly under unstable stratification.
3. Model Suitability by Sector: Sea-sector winds were better represented by models with thermodynamic treatments, while land-sector winds—predominantly neutral and mechanically influenced—showed less distinction across the models. However, residual thermal effects over sea surfaces impacted land-sector winds, suggesting that even nearshore modeling benefits from stability consideration.
4. Atmospheric Stability Variability: Atmospheric stability exhibited significant spatial, temporal, and seasonal variability—particularly during winter—with neutral conditions frequently observed over land and unstable conditions prevailing offshore. These variations influenced the estimation of vertical wind shear and underscore the importance of using stability-aware models in coastal regions.

The results demonstrated that models incorporating atmospheric stability, such as WRF and Meteodyn WT™, produced wind estimations that closely matched in-situ observations and achieved high accuracy. Among these, differences remain in how stability is represented—the mesoscale model dynamically accounts for spatial and temporal changes in atmospheric stability, whereas commercial CFD tools incorporate stability effects through quasi-steady assumptions.

In coastal and nearshore regions, where atmospheric stability varies significantly in both space and time, accurate wind estimation would require simultaneous consideration of both wind flow and stability at each time step. This integrated approach would enable more realistic and stability-aware assessments of offshore wind energy resources.

Although this study was conducted at a specific site in northern Japan, the thermal contrast between land and sea surfaces and its seasonal variability are common in many coastal regions worldwide. Therefore, the findings and methodological approach presented here are considered relevant and applicable to other nearshore wind resource assessments.

The intensive observation campaign in this study was conducted during the cold season, when stable stratification over land and unstable stratification over the sea surface predominated. Therefore, further analysis is necessary to explore the warm season, during which this relationship is reversed. Furthermore, although this study evaluated period-averaged wind speeds, future research should focus on examining finer-scale phenomena, such as turbulence intensity, which is a critical factor in assessing wind turbine fatigue loads. In addition, grid independence testing is recommended to verify the robustness of numerical results, particularly for high-resolution simulations.

Author Contributions: Writing—-original draft and visualization, M.K. (Mizuki Konagaya); review and editing, T.O. and T.M.; supervision, T.O.; conceptualization, data curation, methodology, project administration, and validation, M.K. (Mizuki Konagaya) and T.O.; funding acquisition, M.K. (Mizuki Konagaya), T.O., R.A. and K.H.; formal analysis, M.K. (Mizuki Konagaya) and Y.I.; software and resources, M.K. (Mizuki Konagaya), M.K. (Masaki Kambayashi), E.L., E.T., T.M. and E.S.; investigation, M.K. (Mizuki Konagaya), R.A. and K.H. All authors have read and agreed to the published version of the manuscript.

Funding: This research was funded by the New Energy and Industrial Technology Development Organization (NEDO), Japan (grant number JPNP07015) and partly supported by the Japan Society for the Promotion of Science (JSPS), grant numbers 17H03492 and 22H02018.

Data Availability Statement: Data from the Mutsu Ogawara offshore wind observation test site (St.L, St.$S_{1.5}$, and all the VLs/FLSs) were collected as part of the NEDO project.

Acknowledgments: This research was primarily the result of the NEDO project (JPN07015) and was supported by project members including the National Institute of Advanced Industrial Science and Technology (AIST), Kobe University, E&E Solutions, Inc., Japan Meteorological Corporation, Nippon Kaiji Kyokai (Class NK), and Wind Energy Consulting Inc. The authors are grateful to the above parties for their support in the research and writing of this paper.

Conflicts of Interest: Authors Mizuki Konagaya, Takeshi Misaki, and Erika Shintaku are employed by Rera Tech Inc. Author Yuki Itoshima is employed by ENEOS Renewable Energy Corporation. Author Masaki Kambayashi is employed by Kanadevia Corporation. Authors Edouard Leonard and Eric Tromeur are employed by Meteodyn. Author Ryuzo Araki is employed by Japan Meteorological Corporation. Author Kohei Hamada is employed by E&E Solutions, Inc. The remaining author declares that the research was conducted in the absence of any commercial or financial relationships that could be construed as a potential conflict of interest. In addition, the authors have no intention of influencing the readers' choice or promoting any specific numerical model, including but not limited to those discussed in this article.

Abbreviations

The following abbreviations are used in this manuscript:

CFD	Computational fluid dynamics
FLS	Floating LiDAR system
LiDAR	Light detection and ranging
MASCOT	Microclimate Analysis System for Complex Terrain
MOL	Monin–Obukhov length
NEDO	New Energy and Industrial Technology Development Organization
RANS	Reynolds-averaged Navier–Stokes
SST	Sea surface temperature
VL	Vertical LiDAR
WAsP	Wind Atlas Analysis and Application Program
WRF	Weather Research and Forecasting

References

1. GWEC Global Wind REPORT 2024. 2024. Available online: https://img.saurenergy.com/2024/05/gwr-2024_digital-version_final-1-compressed.pdf (accessed on 27 May 2025).
2. Ninos, E.; Lucas, M.; Ballantyne, J. Japanese Offshore Wind—Status and Recent Developments. Watson Farley & Williams Article. 2024. Available online: https://www.wfw.com/articles/japanese-offshore-wind-developments/ (accessed on 27 May 2025).
3. Konagaya, M.; Ohsawa, T.; Inoue, T.; Mito, T.; Kato, H.; Kawamoto, K. Land–sea contrast of nearshore wind conditions: Case study in Mutsu-Ogawara. *Sola* **2021**, *17*, 234–238. [CrossRef]
4. *Evaluation of Site-Specific Wind Condition*; Version 3; Measurement Procedures; MEASNET: Madrid, Spain, 2022.
5. Skamarock, W.C.; Klemp, J.B.; Dudhia, J.; Gill, D.O.; Liu, Z.; Berner, J.; Wang, W.; Powers, J.G.; Duda, M.G.; Barker, D.M.; et al. *A Description of the Advanced Research WRF Model Version 4*; Tech. Note TN-556+STR; National Center for Atmospheric Research: Boulder, CO, USA, 2021; pp. 1–148. Available online: https://www.ecampmany.com/docs/cheatsheets/WRF.pdf (accessed on 27 May 2025).
6. Misaki, T.; Ohsawa, T. Evaluation of LFM-GPV and MSM-GPV as input data for wind simulation. *J. JWEA* **2018**, *42*, 72–79. [CrossRef]
7. Misaki, T. A Study on Improving the Accuracy of Coastal Wind Speeds Simulated by Mesoscale Model. Ph.D. Thesis, Kobe University, Kobe, Japan, 2020. Available online: https://hdl.handle.net/20.500.14094/D1007801 (accessed on 27 May 2025).
8. Shimada, S.; Ohsawa, T.; Kogaki, T.; Steinfeld, G.; Heinemann, D. Effects of sea surface temperature accuracy on offshore wind resource assessment using a mesoscale model. *Wind Energy* **2015**, *18*, 1839–1854. [CrossRef]

9. Ohsawa, T.; Ishigami, K.; Baba, Y.; Kawaguchi, K. Comparison of WRF-based methods for wind resource assessment at an offshore site. In Proceedings of the Twenty-Fifth International Ocean and Polar Engineering Conference, Kona, HI, USA, 21–26 June 2015.
10. NEDO. The NEDO Offshore Wind Information System. Available online: https://appwdc1.infoc.nedo.go.jp/Nedo_Webgis/top.html (accessed on 27 May 2025).
11. Ohsawa, T.; Uede, H.; Misaki, T.; Kato, M. Accuracy of WRF Simulations Used for Japanese Offshore Wind Resource Maps. In Proceedings of the International Conference on Energy and Meteorology, Bari, Italy, 27–29 June 2017; Available online: http://www.wemcouncil.org/ICEMs/ICEM2017_PRES/ICEM_20170629_1120_Sala_2_Ohsawa.pptx (accessed on 27 May 2025).
12. Kato, M.; Ohsawa, T.; Uede, H.; Shimada, S. Verification of spatial characteristics of WRF-simulated wind speed in Japanese coastal waters. *Proc. Jpn. Wind. Energy Symp.* **2017**, *39*, 253–256. (In Japanese) [CrossRef]
13. Misaki, T.; Ohsawa, T.; Konagaya, M.; Shimada, S.; Takeyama, Y.; Nakamura, S. Accuracy comparison of coastal wind speeds between WRF simulations using different input datasets in Japan. *Energies* **2019**, *12*, 2754. [CrossRef]
14. Makridis, A.; Chick, J. Validation of a CFD model of wind turbine wakes with terrain effects. *J. Wind Eng. Ind. Aerodyn.* **2013**, *123*, 12–29. [CrossRef]
15. Liu, Y.; Ishihara, T. Fatigue Failure Accident of Wind Turbine Tower in Taikoyama Wind Farm. In Proceedings of the EWEA2015, Paris, France, 17–20 November 2015.
16. Kyokai, N.K. Wind Farm Certification Onshore Wind Power Plant Edition. Available online: https://www.classnk.or.jp/hp/pdf/authentication/renewableenergy/en/windfarm/NKRE-GL-WFC01_March2023_Eng_20230331.pdf (accessed on 27 May 2025).
17. NEDO. Offshore Wind Measurement Guidebook. 2023. Available online: https://www.nedo.go.jp/library/fuukyou_kansoku_guidebook.html (accessed on 27 May 2025).
18. Shimada, S.; Kogaki, T.; Konagaya, M.; Mito, T.; Araki, R.; Ueda, Y.; Ohsawa, T. Validation of near-shore wind measurements using a dual scanning light detection and ranging system. *Wind Energy* **2022**, *25*, 1555–1572. [CrossRef]
19. DTU. WAsP Software. Available online: https://www.wasp.dk/ (accessed on 27 May 2025).
20. Lange, B.; Højstrup, J. Evaluation of the wind-resource estimation program WAsP for offshore applications. *J. Wind Eng. Ind. Aerodyn.* **2001**, *89*, 271–291. [CrossRef]
21. Bechmann, A. *WAsP CFD A New Beginning in Wind Resource Assessment*; Technical Report; Riso National Laboratory: Roskilde, Denmark, 2012. Available online: https://www.wasp.dk/software/wasp-cfd (accessed on 27 May 2025).
22. Konagaya, M.; Ohsawa, T.; Mito, T.; Misaki, T.; Maruo, T.; Baba, Y. Estimation of nearshore wind conditions using onshore observation data with computational fluid dynamic and mesoscale models. *Resources* **2022**, *11*, 100. [CrossRef]
23. Takakuwa, S.; Uchida, T. Improvement of airflow simulation by refining the inflow wind direction and applying atmospheric stability for onshore and offshore wind farms affected by topography. *Energies* **2022**, *15*, 5050. [CrossRef]
24. López, G.; Arboleya, P.; Núñez, D.; Freire, A.; López, D. Wind resource assessment and influence of atmospheric stability on wind farm design using Computational Fluid Dynamics in the Andes Mountains, Ecuador. *Energy Convers. Manag.* **2023**, *284*, 116972. [CrossRef]
25. Jimenez, B.; Durante, F.; Lange, B.; Kreutzer, T.; Tambke, J. Offshore wind resource assessment with WAsP and MM5: Comparative study for the German Bight. *Wind Energy* **2007**, *10*, 121–134. [CrossRef]
26. Uchida, T.; Li, G. Comparison of RANS and LES in the prediction of airflow field over steep complex terrain. *Open J. Fluid Dyn.* **2018**, *8*, 286–307. [CrossRef]
27. Beaucage, P.; Brower, M.C.; Tensen, J. Evaluation of four numerical wind flow models for wind resource mapping. *Wind Energ.* **2014**, *17*, 197–208. [CrossRef]
28. Ohsawa, T.; Shimada, S.; Kogaki, T.; Iwashita, T.; Konagaya, M.; Araki, R.; Imamura, H. Progress of NEDO project "Bottom fixed offshore wind farm development support project (Establishment of offshore wind resource assessment method)". *Proc. Jpn. Wind. Energy Symp.* **2020**, *42*, 136–139. (In Japanese)
29. Kobe University. MOC, Mutsu-Ogawara Offshore Wind Observation Test Site. Available online: https://mo-testsite.com/ (accessed on 27 May 2025).
30. Uchiyama, S.; Ohsawa, T.; Asou, H.; Konagaya, M.; Misaki, T.; Araki, R.; Hamada, K. Accuracy verification of multiple floating LiDARs at the Mutsu-Ogawara site. *Energies* **2024**, *17*, 3164. [CrossRef]
31. Wind Cube Vertical Profiler. Available online: https://www.vaisala.com/en/products/wind-energy-windcube (accessed on 27 May 2025).
32. AXYS. WindSentinel. Available online: https://axys.com/flidar-windsentinel/ (accessed on 27 May 2025).
33. Kelberlau, F.; Mann, J. Quantification of motion-induced measurement error on floating lidar systems. *Atmos. Meas. Tech.* **2022**, *15*, 5323–5341. [CrossRef]
34. ZX Lidars. ZX300M. Available online: https://www.zxlidars.com/wind-lidars/zx-300m/ (accessed on 27 May 2025).
35. Uchiyama, S.; Ohsawa, T.; Asou, H.; Konagaya, M.; Misaki, T.; Araki, R.; Hamada, K. Empirical Motion Compensation for Turbulence Intensity Measurement by Floating LiDARs. *Energies* **2025**, *18*, 2931. [CrossRef]

36. Carbon Trust. Offshore Wind Accelerator (OWA), Road Map for the Commercial Acceptance of Floating LIDAR Technology. 2018. Available online: https://ctprodstorageaccountp.blob.core.windows.net/prod-drupal-files/documents/resource/public/Roadmap%20for%20Commercial%20Acceptance%20of%20Floating%20LiDAR%20REPORT.pdf (accessed on 27 May 2025).
37. Lange, B.; Larsen, S.; Højstrup, J.; Barthelmie, R. The influence of thermal effects on the wind speed profile of the coastal marine boundary layer. *Boundary Layer Meteorol.* **2004**, *112*, 587–617. [CrossRef]
38. Gryning, S.E.; Batchvarova, E.; Brümmer, B.; Jørgensen, H.; Larsen, S. On the extension of the wind profile over homogeneous terrain beyond the surface boundary layer. *Boundary Layer Meteorol.* **2007**, *124*, 251–268. [CrossRef]
39. UCAR. Weather Research & Forecasting Model (WRF). Available online: https://www.mmm.ucar.edu/models/wrf (accessed on 27 May 2025).
40. Ishihara, T.; Hibi, K. Numerical study of turbulent wake flow behind a three-dimensional steep hill. *Wind Struct.* **2002**, *5*, 317–328. [CrossRef]
41. Ishihara, T.; Yamaguchi, A.; Fujino, Y. A Nonlinear model for predictions of turbulent flow over steep terrain. In Proceedings of the World Wind Energy Conference and Exhibition, Berlin, Germany, 2–6 July 2002; pp. 1–4.
42. Aqua net. MASCOT. Available online: https://www.aquanet21.co.jp/mascot/ (accessed on 27 May 2025).
43. Mortensen, N.G. *Wind Resource Assessment Using the WAsP Software*; DTU Wind Energy E No. 0135; Technical University of Denmark: Roskilde, Denmark, 2016. Available online: https://backend.orbit.dtu.dk/ws/portalfiles/portal/140943898/Wind_resource_assessment_using_the_WAsP_software_DTU_Wind_Energy_E_0135_.pdf (accessed on 27 May 2025).
44. Meteodyn. Meteodyn WT. Available online: https://meteodyn.com/sectors/onshore-and-offshore-wind-power/meteodyn-universe-wind-farm-development-software/meteodyn-wt-wind-resource-assessment-software/ (accessed on 27 May 2025).
45. Pieterse, J.E.; Harms, T.M. CFD investigation of the atmospheric boundary layer under different thermal stability conditions. *J. Wind Eng. Ind. Aerodyn.* **2013**, *121*, 82–97. [CrossRef]
46. Maruo, T.; Ohsawa, T.; Takakuwa, S.; Hemmi, C.; Watanabe, K.; Hasegawa, S.; Kouso, K.; Shirai, K. Validation of WRF and Vector Equation Method for Nearshore Wind Resource assessment: A Comparison of Accuracy Depending on Input Point Location and Number of Points. *Proc. Jpn. Wind. Energy Symp.* **2023**, *45*, 9–12. (In Japanese) [CrossRef]
47. JMA. Numerical Weather Prediction Activities. Available online: https://www.jma.go.jp/jma/en/Activities/nwp.html (accessed on 27 May 2025).
48. Shimizu, Y.; Ohsawa, T.; Shimada, S. Accuracy validation of offshore wind simulation using WRF with the new SST dataset IHSST. *Proc. Jpn. Wind. Energy Symp.* **2018**, *40*, 167–170. (In Japanese) [CrossRef]
49. Murakami, H. Accuracy estimation of digital map series data sets published by the Geographical Survey Institute. *Geoinformatics* **1995**, *6*, 59–64. [CrossRef] [PubMed]
50. The Ministry of Land, Infrastructure, Transport and Tourism. Data, L.U.M. Available online: http://nlftp.mlit.go.jp/ksj/gml/datalist/KsjTmplt-L03-b.html (accessed on 27 May 2025).
51. EMD International. Chapter 3. WindPRO Knowledge Base—WindPRO 3.6 User Manual. 2022. Available online: https://help.emd.dk/knowledgebase/content/windPRO3.6/c3-UK_windPRO3.6_ENERGY.pdf (accessed on 27 May 2025).
52. Leonard, E.; Li, R.; Tromeur, E.; Dupont, M.; Martellozzo, G.; Gaussorgues, A.; Koutsioumpas, S.; Akcakaya, M. New CFD caliburation methodology for wind resource assessment in highly forested area. In Proceedings of the WindEurope, Bilbao, Spain, 20–22 March 2024. Available online: https://www.youtube.com/watch?v=KRejPD9qVy4 (accessed on 27 May 2025).
53. Copernicus Land Monitoring Service. *Corine Land Cover (CLC) 2018*; Version 20b2—100 m Raster Data; European Environment Agency: Copenhagen, Denmark, 2019. Available online: https://land.copernicus.eu (accessed on 27 May 2025).
54. Li, R.; Leonard, E.; Tromeur, E. Comparison of Three Methods in Atmospheric Stratification Determination. In Proceedings of the WindEurope Brussels, Brussels, Belgium, 23–24 June 2022.